Bioactive Materials 47 (2025) 181–197

Contents lists available at ScienceDirect

Bioactive Materials

journal homepage: www.keaipublishing.com/en/journals/bioactive-materials

Targeting and reprogramming microglial phagocytosis of neutrophils by ginsenoside Rg1 nanovesicles promotes stroke recovery

Kaichao Hu [a,b], Junrui Ye [a], Pinglong Fan [a,c], Ruifang Zheng [d], Shasha Wang [a,e], Ye Peng [a,e], Yuan Ruan [a], Xu Yan [a], Zhao Zhang [a,**], Shifeng Chu [a,***], Naihong Chen [a,b,c,d,e,*]

[a] State Key Laboratory of Bioactive Substances and Functions of Natural Medicines, Institute of Materia Medica & Neuroscience Center, Chinese Academy of Medical Sciences and Peking Union Medical College, Beijing, 100050, China
[b] College of Pharmacy, Changchun University of Chinese Medicine, China, Changchun, 130117, China
[c] Science and Technology Innovation Center, Guangzhou University of Chinese Medicine, Guangzhou, 510405, China
[d] Xinjiang Institute of Materia Medica, Urumqi, 830004, China
[e] Hunan Engineering Technology Center of Standardization and Function of Chinese Herbal Decoction Pieces, College of Pharmacy, Hunan University of Chinese Medicine, Changsha, China

ARTICLE INFO

Keywords:
Stroke recovery
Nanovesicles
Rg1
Neutrophil
Microglia
Neovascularization

ABSTRACT

Stroke remains one of the leading causes of adult disability worldwide, with neovascularization is crucial for brain repair after stroke. However, neutrophil infiltration hinders effective neovascularization, necessitating timely clearance by microglia through phagocytosis. Unfortunately, microglial phagocytic function is often impaired by metabolic defects, hindering post-stroke recovery. Ginsenoside Rg1, derived from Panax ginseng, exhibits neuroprotective properties and regulates cellular metabolism *in vitro* but its therapeutic application is limited by poor brain penetration. Here, we present a targeted delivery system utilizing neutrophil-like cell membrane vesicles (NCM), prepared via nitrogen cavitation, to enhance Rg1 delivery to the brain. These biomimetic vesicles exploit the inherent targeting ability of neutrophil membranes to reach brain injury sites and are subsequently taken up by microglia. Our findings demonstrate that Rg1-loaded vesicles enhance microglial clearance of neutrophils, reduce neutrophil extracellular traps release, and mitigate tissue damage. These effects improve the post-stroke microenvironment, promote vascular remodeling, and ultimately contribute to functional recovery. This strategy highlights the potential of targeted reprogramming microglial cells to enhance their endogenous repair capabilities, offering a promising therapeutic avenue for ischemic stroke management.

1. Introduction

Stroke is recognized globally as the second-leading cause of death and the third-leading cause of disability [1]. Apart from thrombolytic therapies, limited by their narrow therapeutic window and high risk of bleeding [2], stroke patients primarily depend on natural recovery, rehabilitation, and secondary preventive drugs to avoid recurrence. Notably, approximately 75 % of stroke survivors suffer from long-term sequelae [3], significantly diminishing their quality of life and that of their families, while imposing a substantial socioeconomic burden.

Neovascularization plays a crucial role in brain repair after stroke, and hindering this process can worsen the outcome [4–7]. However, the process of angiogenesis after a stroke is often influenced by various factors, preventing effective vascular remodeling [8]. Recent studies have shown that the failure of vascular remodeling after a stroke is largely related to neutrophils and the neutrophil extracellular traps (NETs) they release. NETs release various cytotoxic proteases, such as elastase and MPO, which activate the STING-dependent production of type I IFN-β, damaging endothelial cells and disrupting the blood-brain barrier, and hindering vascular reconstruction and repair after stroke

* Corresponding author. State Key Laboratory of Bioactive Substances and Functions of Natural Medicines, Institute of Materia Medica & Neuroscience Center, Chinese Academy of Medical Sciences and Peking Union Medical College, 2 Nanwei Road, Beijing, 100050, China.
** Corresponding author. State Key Laboratory of Bioactive Substances and Functions of Natural Medicines, Institute of Materia Medica & Neuroscience Center, Chinese Academy of Medical Sciences and Peking Union Medical College, 2 Nanwei Road, Beijing, 100050, China.
*** Corresponding author. State Key Laboratory of Bioactive Substances and Functions of Natural Medicines, Institute of Materia Medica & Neuroscience Center, Chinese Academy of Medical Sciences and Peking Union Medical College, 2 Nanwei Road, Beijing, 100050, China.
E-mail addresses: zhangzhao@imm.ac.cn (Z. Zhang), chushifeng@imm.ac.cn (S. Chu), chennh@imm.ac.cn (N. Chen).

https://doi.org/10.1016/j.bioactmat.2025.01.017
Received 5 August 2024; Received in revised form 8 January 2025; Accepted 15 January 2025

[9–11]. Therefore, the timely and efficient clearance of brain-infiltrating neutrophils may be an effective strategy for improving post-stroke repair [9,12].

Microglial cells play a key role in clearing brain-infiltrating neutrophils. Microglial cells rapidly migrate to the injury site and actively engulf neutrophils in response to neutrophil infiltration, thereby maintaining immune balance [13,14]. Microglial depletion exacerbates neutrophil accumulation and expands ischemic lesions [15], highlighting the critical protective function of microglial phagocytosis against neutrophil-mediated vascular and tissue damage in cerebral ischemia. Our previous research found that continuous stimulation by chemokines after stroke causes metabolic defects in microglia, leading to microglial immune tolerance and impairing the phagocytosis and clearance of neutrophils. This aggravates the neuroinflammatory response and worsens the long-term outcomes of ischemic stroke [16]. Therefore, specifically training and empowering microglial cells in the damaged brain to enhance their phagocytic function is crucial for timely neutrophil clearance and improving post-stroke repair [14].

Ginsenoside Rg1, a triterpene saponin and the main active ingredient of the traditional Chinese medicines Panax ginseng and Panax notoginseng [17], has antioxidant properties and regulates energy metabolism. It can alleviate cerebral ischemic injury and holds great potential for the treatment of ischemic stroke [18–20]. However, previous studies have shown that Rg1 exhibits poor absorption, rapid elimination and low brain tissue concentrations due to the blood-brain barrier (BBB), requiring very high doses to achieve therapeutic effects in animal models [17,21,22]. While liposomal delivery systems can facilitate the transport of Rg1 across the BBB, these approaches lack the precision delivery to microglial cells in the brain [23,24]. Therefore, finding a delivery strategy to enhance Rg1 brain penetration and target phagocytic microglial cells to regulate their energy metabolism is crucial for its further investigation. After ischemic stroke, the crosstalk between peripheral immune cells and brain-resident cells mediated by the inflammatory response is a crucial pathological feature [25]. Neutrophils are among the first peripheral immune cells to respond to inflammatory signals and infiltrate the brain [26,27]. Upon activation by inflammatory cytokines, neutrophils express proteins such as integrin β2 and P-selectin glycoprotein ligand-1 (PSGL-1), which enable their binding to intercellular adhesion molecule-1 (ICAM-1) and vascular cell adhesion molecule-1 (VCAM-1) expressed by inflammatory cerebral endothelial cells, facilitating their infiltration into the brain parenchyma [28,29]. Inspired by this mechanism, a targeted delivery method involving neutrophil membrane encapsulation has emerged. This method retains the binding ability of neutrophils to cerebral endothelial cells while eliminating their inflammatory functions [30]. In this study, we prepared neutrophil-like cell membrane vesicles utilizing nitrogen cavitation. These vesicles leverage the targeting capability of neutrophil membranes to deliver drugs to injury sites. Once taken up by microglial cells, Rg1-loaded vesicles significantly enhance the microglial phagocytosis of neutrophils, reducing NETs release and mitigating tissue damage in the infarct zone. This approach improves the post-stroke microenvironment, promotes vascular remodeling, and facilitates functional recovery, presenting a novel strategy for targeted training and reprogramming of microglial cells to enhance their endogenous post-stroke repair capability.

2. Methods

2.1. Materials

The sources of antibodies, chemicals, assay kits, and instruments used in this study are listed in Supplementary Table S1.

2.2. Cell culture

HL-60 cells were cultured in IMDM supplemented with 20 % fetal bovine serum (FBS), and 1 % penicillin/streptomycin. BV2 cells were cultured in DMEM supplemented with 10 % FBS, and 1 % penicillin/streptomycin. These cells were cultured at 37 °C in a 5 % CO_2 incubator and passaged every two days.

2.3. Preparation of neutrophil-like cell membrane-derived extracellular vesicles

HL-60 cells were cultured in a complete IMDM containing 1.25 % DMSO for 5 days to induce differentiation. Cells were pelleted by centrifugation at 400 g for 10 min, washed three times with HBSS (without Ca^{2+} and Mg^{2+}), and resuspended in HBSS (containing 2 mM $MgCl_2$). Cells were then disrupted by nitrogen cavitation at 350–400 psi for 20 min to disrupt the cells, repeated twice. The suspension was centrifuged at 2000 g for 30 min at 4 °C to remove the cell nuclei. EDTA (2.5 mM) was added to the supernatant and subjected to ultracentrifugation at 100,000 g for 30 min at 4 °C, repeated twice, to obtain nanovesicles. The nanovesicles were freeze-dried for 1 h and stored at −20 °C.

2.4. Preparation of Rg1/DiD/Dil@NCM and the loading efficiency and release study

Nanovesicle suspensions were heated to 37 °C and the pH value was adjusted to 4.5 for drug loading. Rg1 and nanovesicles were quickly mixed at a ratio of 10 mg/mL (Rg1) and 30 mg/mL of nanovesicles, followed by sonication for 2 min on ice, and incubated at 37 °C for 30 min. The suspension was centrifuged at 100,000 g for 30 min at 4 °C to remove free Rg1 and obtain drug-loaded vesicles. DiD/Dil and nanovesicles were quickly mixed at a ratio of 100 mM (DiD/Dil) and 4 mg nanovesicles, followed by sonication for 2 min on ice, and incubated at 37 °C for 30 min. The suspension was centrifuged at 100,000 g for 30 min at 4 °C to remove free Did/Dil. The amount of loaded Rg1 in vesicles was analyzed using HPLC/MS (Agilent 1290II-6460) to calculate encapsulation efficiency (EE) and drug loading (DL). EE (%) = Weight of loaded Rg1/Weight of total Rg1 × 100 % [31]. DL (%) = Weight of loaded Rg1/Weight of NCM [32]. In the release study, the prepared Rg1@NCM were resuspended in a PBS solution containing 20 % FBS, evenly distributed into several tubes, and centrifuged at 100,000 g at different time points to obtain pellets. Then methanol was used to extract Rg1 from the nanovesicles. Extracted Rg1 was analyzed by HPLC/MS. In the HPLC experiment, the mobile phase (acetonitrile: water: acetic acid = 15:85:0.01) was used at a flow rate of 0.25 mL/min. The chromatographic conditions were as follows: chromatographic column: Waters BEH C-18 (2.1×10 mm 1.7 μm), column temperature: 40 °C, flow rate: 0.25 mL/min. Mass spectrometry conditions were as follows: ion source: +ESI electrospray ion source, IS: +4000 V (spray voltage), GS1: 45 psi (atomizing gas), scan mode: MRM multiple reaction monitoring CAD: 3 Medium (collision gas), TEM: 350 °C (atomization temperature).

2.5. Characterization of NCM

After staining with 1 % phosphotungstic acid, the morphology of the nanovesicles was observed using transmission electron microscopy (TEM) (JEM-1200EX, JEOL, Japan). After diluting the sample to 0.5 mg/mL with PBS (pH 7.4), the hydrodynamic size and zeta potential of NCM and Rg1@NCM were characterized at 25 °C using the Zetasizer Nano ZS (Malvern, UK). The membrane proteins of NCM and Rg1@NCM were identified using Western blot analysis with antibody PSGL-1 and Integrin β2.

2.6. Animals

SPF-grade male C57BL/6J mice (9 weeks old, weight = 23 ± 2 g) were purchased from Beijing SPF Biotechnology Co., Ltd. The mice were

housed in a 12-h light/dark cycle and had ad libitum access to water and standard laboratory chow. All animal protocols were approved by the Ethics Committee of the Animal Center of the Chinese Academy of Medical Sciences. All animal care and experimental procedures complied with the principles outlined in the NIH Guide for the Care and Use of Laboratory Animals and were approved by the Institutional Animal Care and Use Committee of the Peking Union Medical College and Chinese Academy of Medical Sciences (Ethics number: 00007889).

2.7. Photothrombotic stroke model

The operational procedures for the PT model were based on previous research [16]. The surgery was performed under 2 % isoflurane anesthesia, and the mice were fixed using a stereotaxic frame (RWD Life Science, China). The rectal temperature was maintained at 37.0 ± 0.5 °C using a heating pad. The skull was exposed, and the right M1 area of the brain was marked for photothrombotic stroke induction. A hole was drilled at the coordinates AP, +1.5 mm; ML, −2.0 mm; DV, −1.7 mm, and 200 μL of 10 mg/mL Rose Bengal solution (Solarbio, China) was administered through the tail vein. After 5 min, the M1 area of brain was exposed to a green laser beam with a diameter of 2 mm (wavelength 532 nm) for 8 min to induce ischemia in this specific brain area.

2.8. Transient middle cerebral artery occlusion (tMCAO) model

Anesthesia was induced with 3 % isoflurane and maintained at 1.5 % isoflurane. The left common carotid artery was exposed, and a silicone-coated 6–0 nylon suture was advanced along the internal carotid artery to the bifurcation of the internal and middle cerebral arteries, and left in place for 1.5 h to induce occlusion. After the occlusion period, the suture was removed to restore blood flow to the middle cerebral artery area. The temperature of mice was maintained at 37.0 ± 0.5 °C during the surgery and recovery period using a temperature-controlled heating pad.

2.9. Ex vivo brain and other organs imaging and quantification

Brain tissue (both hemispheres), and other organs (heart, spleen, lung, kidney, and liver) were collected 1 h after injection of free DiD dye or NCM@DiD, which was administered 2 h following PT surgery. The tissues were imaged under an *in vivo* imaging system (IVIS). Afterward, tissues were collected and homogenated in PBS buffer, and fluorescent signals of DiD were measured by a microplate reader.

2.10. In vivo multiphoton microscopy

Following 2 h reperfusion post-tMCAO, mice received an intravenous injection of Dil@NCM (red) via the tail vein. Anesthesia was administered using 1.5 % isoflurane in a mixture of 30 % oxygen and 70 % nitrous oxide. Throughout the procedure, mice were maintained at normothermia on a heating plate regulated to 37 ± 0.5 °C. The animals were then securely positioned in a custom-designed head holder. A craniotomy was performed over the left somatosensory cortex, centered at coordinates 2.5 mm lateral and 1.5 mm posterior to the bregma, using a high-speed micro drill. To complete the preparation of the imaging window, a sterile cover glass was positioned over the exposed area and affixed with dental cement. Subsequently, FITC-Dextran-2000 (green) was administered intravenously. *In vivo* imaging was conducted through the cranial window using an upright multiphoton laser-scanning microscope (FluoView FVMPE-RS, Olympus, Japan). Two-photon excitation was generated using MAITAI eHPDS-OL and Spectra Physics InSight DS-OL lasers (Mai Tai, Spectra-Physics, Santa Clara, CA).

2.11. Measurement of Rg1 content in brain tissue

After 2 h of PT modeling, administer 40 mg/kg of free Rg1 or Rg1@NCM containing an equal dose of Rg1. 1 h later, brain samples were taken from both hemispheres and added to 200 μL of methanol-water (1:1), vortexed for 10 min, sonicated (40 kHz) for 2 min, and then centrifuged at 13,200 rpm for 4 min. A 50 μL aliquot of the supernatant was taken and added to 150 μL of the organic phase for precipitation, vortexed for 1 min, and then centrifuged at 13,200 rpm for 4 min. A 50 μL aliquot was taken for analysis using high-performance liquid chromatography-triple quadrupole mass spectrometry (HPLC-MS/MS) (AB API3200MD) to detect the content of Rg1. The liquid phase conditions were as follows: chromatographic column: MSLab C18 (100×4.6 mm 2.5 μm), column temperature: 50 °C, flow rate: 1.0 mL/min. Mobile phase: (A) organic phase: methanol + acetonitrile (8:2) (ammonium acetate + formic acid) (B) aqueous phase: water (ammonium acetate + formic acid), injection volume: 10 μL. Mass spectrometry conditions were as follows: ion source: + ESI electrospray ion source IS: +5000 V (spray voltage), GS1: 50 psi (atomizing gas), GS2: 60 psi (auxiliary gas), scan mode: MRM multiple reaction monitoring CAD: 3 medium (collision gas), TEM: 550 °C (atomization temperature), CUR: 20 psi (curtain gas), CXP: +2.0 (collision chamber ejection pressure), EP: +10 (injection voltage).

2.12. Magnetic resonance imaging data collection and analysis

Infarct volume analysis. MRI data sets were generated on a PharmaScan 70/16 (Bruker BioSpin, Ettlingen, Germany), and image acquisition was collected using ParaVision_6.0.1 software (Bruker BioSpin GmbH). Anesthesia was induced with 5 % isoflurane and then maintained at 1.5 % isoflurane throughout the experiment. T2-weighted sequences were applied for visualization of the infarction, with detailed parameters as follows: field of view (FOV) = 20 × 20 mm, echo time (TE) = 15 ms, repetition time (TR) = 2 s, acquisition matrix = 64 × 64, 25 coronal slices, slice spacing of 0.5 mm, and slice thickness of 0.05 mm. The data was viewed and the infarct area was calculated using Radiant Dicom Viewer software. The infarct rate was calculated as follows: [total area of damage/(total area of contralateral hemisphere × 2)] × 100 %.

Functional MRI data analysis. At the beginning of each MRI examination, FieldMap and continuous local shimming were used to improve the homogeneity of the magnetic field. Subsequently, a T2-weighted TurboRARE sequence was used as an anatomical reference scan, followed by the acquisition of functional MRI using a free induction decay echo-planar imaging (FID-EPI) sequence, repeated 300 times. The field of view (FOV) was 20 × 20 mm^2, with 40 slices, a thickness of 0.35 mm, and an interslice gap of 0.05 mm. The matrix size was 64 × 64, with a repetition time (TR) of 2000 ms and an echo time (TE) of 15 ms. Brain functional data sets were extracted and the original data was converted to NIfTI format files using dcm2nii. Voxel size was increased by 10 times, and time slice correction was performed with the middle layer as the reference layer. Re-alignment was conducted to align each subject's time-processed volume to the mean volume to eliminate any head motion. An average image was created from the 300 realigned volumes. After head motion correction, all subject data was registered to standard space using a two-step registration method with the ANTS (1.9.2) toolkit. Functional images were registered to the Allen Mice Brain using T2 and mean function images. Gaussian smoothing (smoothing kernel = 6 mm) and filtering (range 0.01–0.08 Hz) were then performed on the registered data using SPM12 and rest plus V1.2.8–130615 toolkits. Subsequently, regression covariate analysis and detrend analysis were performed to obtain the data for analysis. The filtered time series were transformed into the frequency domain using the Fourier transform, and the power spectrum was calculated in the 0.01–0.08 Hz range, with the square root representing the amplitude of low-frequency fluctuations (ALFF). Each voxel's ALFF value was divided by the mean of all voxel ALFF values to obtain the standardized average ALFF value. Similarly, ReHo values were obtained using the REST software. Functional connectivity between regions of interest (ROIs) was analyzed, with the

following brain areas selected: primary motor area (MO), primary somatosensory area (SSp), supplementary somatosensory area (SSs), prelimbic area (PL), and superior colliculus (SC), which are closely related to post-stroke motor symptoms. The correlation coefficients between seed points were calculated and then Fisher-z normalized to obtain zFC. Statistical analysis was performed using MATLAB R2013b (The MathWorks, Inc., Natick, Massachusetts, United States). Brain Net Viewer (v1.61) was used to visualize the functional connectivity results.

2.13. Behavioral tests

Behavioral tests were conducted before and 1, 3, 7, 14, and 28 days after the stroke.

Grid walking test. Forelimb motor function was assessed using the number of foot faults in the grid walking test. Mice were placed on a square grid measuring 50 cm × 50 cm, with each small grid measuring 3 cm × 3 cm. Mice were placed in the center of the grid and allowed to crawl for 1 min. The number of times the left forelimb did not provide support or slipped through the grid holes and the total steps of both forelimbs were recorded. The test was repeated three times with a 1-min interval. The error rate was calculated as the number of errors in the left forelimb (injured side) divided by the total steps of both forelimbs.

Cylinder test. Mice were placed in a transparent cylindrical container (D × H: 15 cm × 20 cm) and allowed to move freely. Each time an upper limb made contact with the cylinder wall in an upright position until the end (marked by the return of both upper limbs to the ground) was counted as one action, and the first 20 actions were recorded. The bias was calculated as: (time spent using the right forelimb independently - time spent using the left forelimb independently)/(number of times the right forelimb + number of times the left forelimb + number of times both forelimbs were used).

2.14. Immunofluorescence

Brain was fixed with 4 % PFA for 24 h, dehydrated with gradient sucrose, and 25 μm frozen brain sections were obtained using a cryostat. The sections were incubated with primary antibodies: *anti*-Iba1, *anti*-GFAP, *anti*-Olig2, anti-CD31, *anti*-Ly6G, or *anti*-NeuN overnight at 4 °C. After washing with PBS, the sections were incubated with secondary antibodies: donkey anti-rabbit Alexa Fluor 594 or goat anti-mice Alexa Fluor 488 (Invitrogen, 1:500), at room temperature for 2 h. The cell nuclei were stained with DAPI. Images were acquired using a BioTek Cytation C10 confocal microscope.

2.15. Microglial isolation from adult mice brains

Mice were injected with NCM or Rg1@NCM via the tail vein after PT modeling. Mice were euthanized 3 days later, after which microglia were isolated from the mouse brains. Briefly, brains were incubated in ice-cold Dulbecco's PBS (dPBS; Sigma-Aldrich, USA). The tissue of the injured side (excluding the olfactory bulb and cerebellum) was mechanically dissociated and enzymatically digested using a gentleMACS Dissociator (Miltenyi Biotec, Germany) with the program Brain-01-03. The cell suspension was filtered through a 70 μm cell strainer (Falcon) to obtain a single-cell suspension. Debris was removed using a fragment removal solution. Microglia were isolated using CD11b microbeads (Miltenyi Biotec, Germany) and magnetic-activated cell sorting. Isolated microglia were lysed with ice-cold TRIzol reagent and stored at −80 °C.

2.16. RNA sequencing of microglia

Total RNA was extracted from the isolated microglia and subjected to RNA quality testing, and messenger RNA was purified by mRNA-specific polyA structure using the TruSeq Stranded mRNA LT Sample Prep kit (Illumina). cDNA libraries were prepared by reverse transcription, double-strand synthesis, end-repair, A-tailing, and adapter ligation. Libraries were size-selected using magnetic beads, pooled, diluted to 2 nM, and denatured. Sequencing was performed on the NovaSeq 6000 PE150 platform. Filtering was performed to obtain high-quality clean data by comparing the clean data with a designated reference genome, calculating the comparison efficiency of the sequencing data with the reference genome, and evaluating the saturation of the sequencing data and the gene coverage. Differential genes were screened in different sample groups, and visualized displays such as clustering analysis and volcanic diagrams were conducted on the differential genes. GO/KEGG functional annotation and functional enrichment analysis were conducted on the differential genes to examine the functions and regulatory relationships of the differential genes.

2.17. Western blot

Brain tissue was collected from the injured hemisphere 3 days after PT and total protein was extracted using RIPA lysis buffer containing a mixture of protease and phosphatase inhibitors and quantified using a BCA protein assay kit. The proteins were separated by 10 % SDS-PAGE gel electrophoresis and transferred to a PVDF membrane (Merck Millipore, USA). After blocking with 5 % bovine serum albumin (BSA) in Tris-buffered saline with 0.1 % Tween-20 (TBS-T) at room temperature (RT) for 2 h, the membrane was then incubated overnight at 4 °C with the following primary antibodies including PSGL-1 (A23373, Abclonal), Integrin β2 (A19012, Abclonal), AMPK α1 + AMPK α2 (ab131512, Abcam), AMPK α1 (phospho T183) + AMPK α2 (phospho T172) (ab133448, Abcam), CD68(ab283654, Abcam), Ly6G (551459, BD Biosciences), NE (sc-55549, Santa Cruz), MPO (ab90810, Abcam), H3Cit (ab5103, CST), Histone H3 (9715S, Abcam), cGAS (26416–1, Proteintech), STING (19851-1-AP, Proteintech), pTBK1 (5483S, CST), TBK1 (28397, Proteintech), pIRF-3 (Ser396) (29047s, CST), IRF3 (66670-1-AP, Proteintech), IL-6 (ab208113, Abcam), ZO-1 (40–2200, Thermo Fisher Scientific), Occludin (A2601, ABclonal), GAPDH (60004, Proteintech), β-actin (AC038, ABclonal). After washing 3 times, species-specific horseradish peroxidase-conjugated sheep anti-rabbit IgG (5220–0336, SeraCare) or horseradish peroxidase-polyclonal sheep anti-mouse IgG (5220–0341, SeraCare) for 2 h at 25 °C. The expression of each protein was examined using an enhanced chemiluminescence detection system. Data analysis was performed using FIJI software, and the results were presented as normalized to controls for each experiment.

2.18. Primary bone marrow-derived neutrophils culture

Bone marrow cells were isolated from the femurs and tibia of healthy C57BL/6J donors. The cell suspension was subjected to gradient density ultracentrifugation with a percoll density of 80, 65, and 55 %. A cell layer between 65 and 55 % percoll was collected to obtain neutrophils. The neutrophils were cultured in a complete DMEM.

2.19. Phagocytosis assay in vitro

BV2 microglia were cultured overnight in 24-well plates. After 3 h of OGD, PBS or NCM (2 μg/mL) or Rg1@NCM (2 μg/mL) or Rg1@NCM (2 μg/mL) + Compound C (2 μg/mL) were added into the cell culture system for 12 h at 37 °C. Next, neutrophils co-cultured with microglia at a ratio of 3:1 (neutrophils: microglia) for 6 h at 37 °C. Then, microglia were washed with PBS to remove the suspended neutrophils. For confocal microscopy analysis, cells were stained with Iba1 and Ly6G antibodies, and the phagocytosis of neutrophils by microglia was checked with a confocal microscope. For Western blot analysis, the proteins of the co-culture system were collected, and the neutrophils phagocytosed by microglia were detected by examining the Ly6G, CD68, and p-AMPK/AMPK expression. Furthermore, microglia were collected into tubes and stained with CD16/32 and Ly6G-PE antibodies for 30 min at 4 °C. Flow cytometry analysis was conducted to detect the ratio of

microglial phagocytosis using Amnis ImageStream Imaging Flow Cytometer and IDEAS analysis.

2.20. Seahorse assay

Seahorse XF Cell Mito Stress Test Kit and the Seahorse Extracellular Flux (XF24) Analyzer were used to analyze cell bioenergetics. Microglia (4×10^4 cells/well) were seeded on Seahorse cell culture microplates and incubated in DMEM. After OGD/R and drug treatments, the oxygen consumption rate (OCR) was measured according to the manufacturer's protocol. For the OCR test, oligomycin (2 μM), FCCP (2 μM), and antimycin A (2 μM) were loaded into the appropriate ports for sequential delivery. Following calibration, OCR was measured at 8-min intervals over a 96-min period, with the appropriate compounds were injected sequentially. OCR was automatically calculated using the Seahorse XF24 software, and 4 replicates were assessed for each separate sample.

2.21. Vessel analysis

PT modeling after 14 days, 50 μL of 5 % TRITC 155 kDa (T1287, SIGMA) was injected into the tail vein. After 15 min, the brain was collected, and 100 μm thick sections were placed in a custom brain slot. The Z-axis images were scanned using a Cytation C10 confocal microscope to a depth of 60 μm, and the vessel density was analyzed using the VESSELJ V 1.0 plugin in FIJI software. Vessels were reconstructed using the filament plugin in IMARIS 9.0.1 software, and vessels with diameters less than 6 μm were screened for microvascular and analyzed for length, area, and volume of microvascular.

2.22. Cytotoxicity assay in vitro

BV2 cells were cultured in 96-well plates at a density of 5×10^3 per well and incubated with NCM at different concentrations (0, 0.4, 2, 10, 50, and 250 μg/mL) at 37 °C for 48 h. Subsequently, each well was rinsed with PBS, replenished with 90 μL of serum-free medium and 10 μL

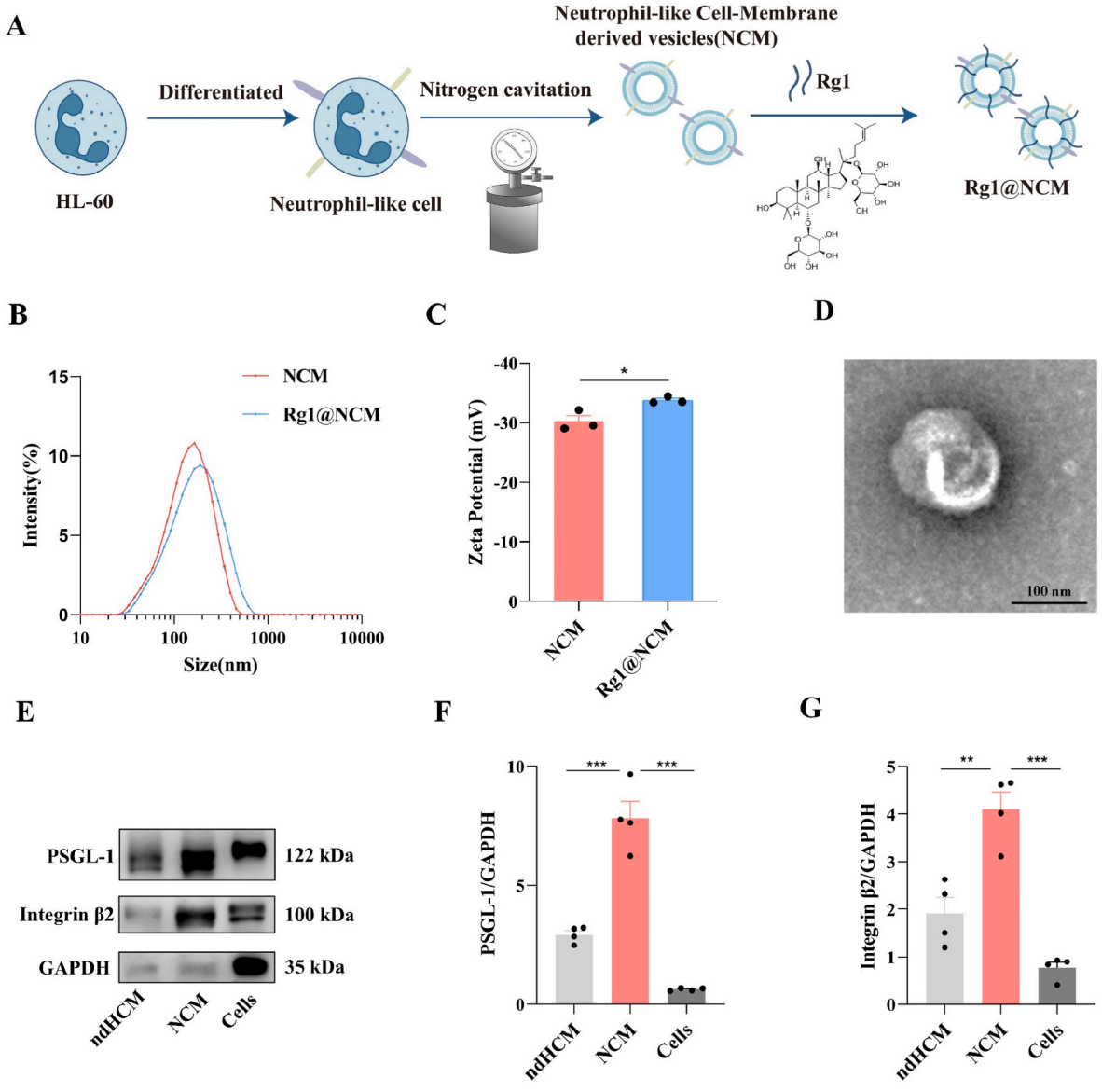

Fig. 1. Characterizations of Rg1@NCM. (A) Schematic design of the preparation of Rg1@NCM. (B) Size distribution and (C) Zeta potentials of NCM and Rg1@NCM. (n = 3). (D) Representative image of Rg1@NCM observed by transmission electron microscopy. Scale bar = 100 nm. (E) Western blot analysis of PSGL-1 (F) and integrin β2 (G) on nondifferentiated HL-60 cell membrane vesicles (ndHCM), differentiated neutrophil-like cell membrane vesicles (NCM) and differentiated HL-60 cells (Cells). (n = 4). *$P < 0.05$, **$P < 0.01$, ***$P < 0.001$.

of CCK-8, and incubated for another 1.5 h at 37 °C. The absorbance of each well was measured at 450 nm by a microplate reader (SpectraMax ID5, Molecule Devices, USA).

2.23. Quantification and statistical analysis

All statistical tests were performed using GraphPad Prism 8.0. All the results were shown as the mean ± SEM from at least three independent experiments. The unpaired two-tailed Student's *t*-test was used to analyze the experiments with only two groups. For experiments

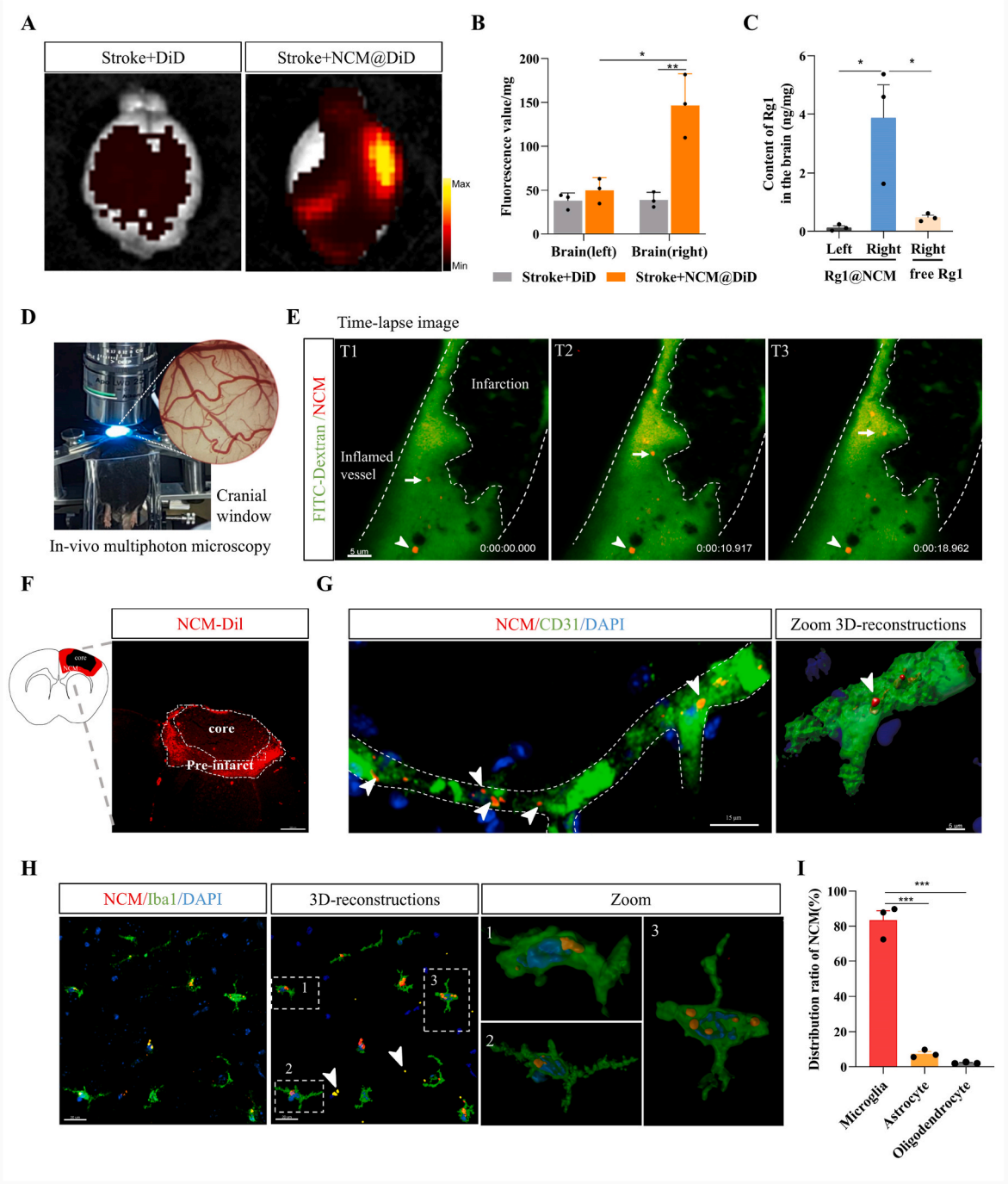

Fig. 2. The NCM targeted stroke-injured regions. (A) *Ex vivo* brain images taken 1 h after injection of either free DiD or NCM@DiD in a PT stroke mice model. (B) Fluorescence intensity of DiD in homogenized brain tissues (n = 3). (C) The content of Rg1 in the left and right hemispheres of PT stroke mice injected with Rg1@NCM or free Rg1, determined by HPLC-MS/MS (n = 3). (D, E) Real-time *in vivo* multiphoton microscopy images showing the microcirculation in a live mouse brain. After MCAO surgery, several Dil-labeled NCM (red) bound to inflamed brain vasculature, with FITC-Dextran-2000 (green) administered intravenously to label blood vessels. No-tailed arrows indicate NCM remaining in the inflamed blood vessels, while tailed arrows indicate the NCM aggregating towards the injury site. Scale bar = 5 μm. (F) Distribution of NCM (Dil^+) in PT-injured regions at 1 h post-intravenous injection. (G) Immunofluorescence observation of NCM (Dil^+) binding with endothelial cells ($CD31^+$). Scale bar = 15 μm (left), 5 μm (right). (H) Representative immunofluorescence fluorescence images and 3D reconstruction showing NCM (Dil^+) internalized by microglia ($Iba1^+$) at 3 h post-intravenous injection. The 3D reconstruction highlights NCM internalized by microglia in red and NCM uninternalized by microglia in yellow. Scale bar = 20 μm. (I) Ratio of NCM internalized by different cells (n = 3). $^*P < 0.05$, $^{**}P < 0.01$, $^{***}P < 0.001$.

comparing more than two groups, one-way analysis of variance (ANOVA) followed by Tukey's *post hoc* test for multiple comparisons was used. Statistical significance was defined as $P < 0.05$ in all analyses.

3. Results

3.1. Construction and characterization of Rg1@NCM

In this study, NCM were generated from differentiated HL-60 cells using nitrogen cavitation. Rg1 was then loaded into the NCM, and free Rg1 was removed by centrifugation (Fig. 1A). HPLC-MS analysis revealed an Rg1 encapsulation efficiency of 32.6 %. The size and zeta potential of the vesicles were measured using dynamic light scattering. The NCM exhibited an average particle size of 122.0 nm with a PDI of 0.24. After Rg1 encapsulation, the average particle size increased to 143.2 nm (PDI 0.29) (Fig. 1B). The zeta potential of the vesicles was observed to be −30.2 mV, which increased to −33.8 mV after loading Rg1 to the nanovesicles, suggesting that Rg1 may be incorporated into the lipid bilayer of the vesicles (Fig. 1C). Transmission electron microscopy revealed the morphology of the nanovesicles, which appeared as regular spherical structures with a diameter of approximately 140 nm (Fig. 1D). Rg1@NCM released 88 % of Rg1 within 24 h in a 20 % FBS solution (Fig. S1A), suggesting that Rg1 may tightly be incorporated in nanovesicles when they are used for *in vivo* studies. In addition, the changes in particle size and potential of Rg1@NCM in a 20 % FBS solution were monitored over 48 h. It was found that the particle size of Rg1@NCM did not change significantly within 24 h, indicating that Rg1@NCM may be stable (Fig. S1B). Western blot analysis confirmed the membrane protein enrichment in the NCM. Compared to differentiated HL-60 cells, the NCM showed 6.3-fold lower GAPDH levels (10 μg total protein), indicating reduced intracellular protein contamination. PSGL-1 and integrin β2 on neutrophils are involved in the binding of neutrophils to inflamed endothelial cells [28]. The ratios of PSGL-1/GAPDH and integrin β2/GAPDH in differentiated vesicles were approximately 12.6 times and 5.3 times that in differentiated HL-60 cells, respectively, confirming the enrichment of cell membrane components. Additionally, these ratios were approximately 2.7 times and 2.1 times that in nondifferentiated HL-60 cell membrane vesicles (ndHCM), implying that differentiated neutrophil membrane vesicles possess a greater potential to bind to inflamed vascular endothelial cells (Fig. 1E–G).

3.2. Targetability of Rg1@NCM to the injured brain after stroke

In vivo, the targetability of NCM to an inflamed brain after a stroke was assessed using a mice stroke model of photothrombosis (PT). NCM were labeled with the far-red fluorescent lipid dye DiD. Mice were injected intravenously (i.v.) with NCM@DiD or free DiD 2 h after PT. One hour after injection, the brain (Fig. 2A) and other organs (Fig. S2) were imaged using an *in vivo* imaging system (IVIS). The content of DiD in the homogenized tissues was also measured. The results indicated that the accumulation of NCM@DiD in the injured right brain was significantly higher than in the uninjured left brain (Fig. 2B). To verify whether NCM can enhance the targeted delivery of Rg1 across the BBB to the lesion site, Rg1 (40 mg/kg) or an equal dose of Rg1@NCM was intravenously injected via the tail vein 2 h post-PT. HPLC-MS/MS analysis of brain tissue 1 h post-injection showed that Rg1@NCM group resulted in an 8-fold higher Rg1 concentration (3.87 ng/mg) in the injured right hemisphere compared to free Rg1 group (0.48 ng/mg) (Fig. 2C). This suggests that NCM has great inflammatory targetability and can effectively help Rg1 cross the BBB, thereby increasing the amount of Rg1 in the brain.

To further observe the interaction between NCM and cells in the brain, *in vivo* multiphoton microscopy was used to live-imaging the presence of NCM in the brain vessels of the mice after MCAO, another stroke model. Two hours after reperfusion, mice received Dil-labeled NCM i.v., and blood vessels were visualized with FITC-dextran (2000 kDa) (Fig. S3A). Multiphoton microscopy revealed the gradual accumulation and binding of Dil-labeled NCM to the vessel walls in the perilesional area (Fig. 2E–Supplementary Movie 1; white arrow indicates binding). In the PT mice, Dil-labeled NCM was injected intravenously via the tail vein 2 h after PT. One hour after injection, the mice were euthanized, brain tissue was sectioned and immunofluorescence stained, and fluorescence images were captured using Cytation C10. As shown in Fig. 2F, Dil-labeled NCM was observed to accumulate in the perilesional area of the PT infarction. In the injury area, the red Dil-labeled NCM was observed to bind to endothelial cells ($CD31^+$) (Fig. 2G). Three hours post-injection, brain slices were obtained similarly, and immunofluorescent staining was used to label microglia ($Iba1^+$), astrocytes ($GFAP^+$), and oligodendrocytes ($Olig2^+$) (Fig. 2H, Fig. S4). A 3D reconstruction with Imaris revealed approximately 82 % of NCM colocalized with microglia (Fig. 2I). Besides, NCM binding to blood vessels in the injured region (Fig. S3B) and colocalization with microglia (Fig. S3C) in tMCAO mice were also observed by immunofluorescence. These results demonstrate that Rg1@NCM can reach the site of brain injury in two stroke mice models and can be taken up by microglia in both models.

3.3. Rg1@NCM alleviates brain tissue damage and promotes long-term neurological functional recovery post-stroke

The effects of Rg1@NCM on brain injury and functional recovery in PT mice were investigated. Two hours after PT surgery, PBS, NCM, free Rg1 (10 mg/kg), or an equal dose of Rg1@NCM was intravenously injected via the tail vein (Fig. 3A). Structural MRI scans were performed on day 3 (Fig. 3B) and day 28 (Fig. 3E) after PT modeling. For visual observation, 3D reconstructions were reconstructed from MRI images. White represents the healthy brain tissue, red represents infarct brain tissue (Fig. 3C–F). After 3 days, the infarction rate was 11.04 % in the PT group and 6.00 % in the Rg1@NCM group. No significant reduction was observed in the free Rg1 or empty NCM groups (Fig. 3D). After 28 days, the Rg1@NCM group showed a significantly reduced infarction rate (0.30 %) compared to the PT, free Rg1, and empty NCM groups (approximately 20–26 % of the infarction rate in these groups) (Fig. 3G). This indicates that the Rg1@NCM treatment demonstrated significantly enhanced post-stroke repair efficacy compared to the other groups. Behavioral studies were performed on days 1, 3, 7, 14, and 28 after PT stroke. In the grid-walking test, animals treated with Rg1@NCM performed better than the PT group on all tested days, with a significantly reduced chance of dropping the left forelimb (Fig. 3H). Similar results were observed in the cylinder test, where animals injected with Rg1@NCM showed less deviation on days 1, 3, 7, 14, and 28 after PT stroke (Fig. 3I). The behavioral performance of the NCM group and the free Rg1 group did not show significant improvement compared to the PT group. From the results above, the Rg1@NCM treatment significantly reduced cerebral infarction volume and enhanced long-term motor function recovery in mice, demonstrating superior efficacy compared to free Rg1 at an equivalent dose. These findings suggest the NCM nanocarrier effectively enhanced the therapeutic potential of Rg1.

3.4. Rg1@NCM enhances long-term functional connectivity in sensorimotor and cognitive-associated regions post-stroke

To assess the impact of Rg1@NCM on restoring brain functional connectivity after stroke, we conducted fMRI scans 28 days post-stroke. We then analyzed differences in regional aberrant amplitude of low-frequency fluctuations (ALFF) and regional homogeneity (ReHo) between the Rg1@NCM and NCM treatment groups. ALFF represents the amplitude of spontaneous neuronal activity in the region, while Reho represents the coordination of regional neural activity [33]. Compared to the NCM group, the Rg1@NCM group exhibited increased ALFF values in several brain regions, including the primary motor area (MOp),

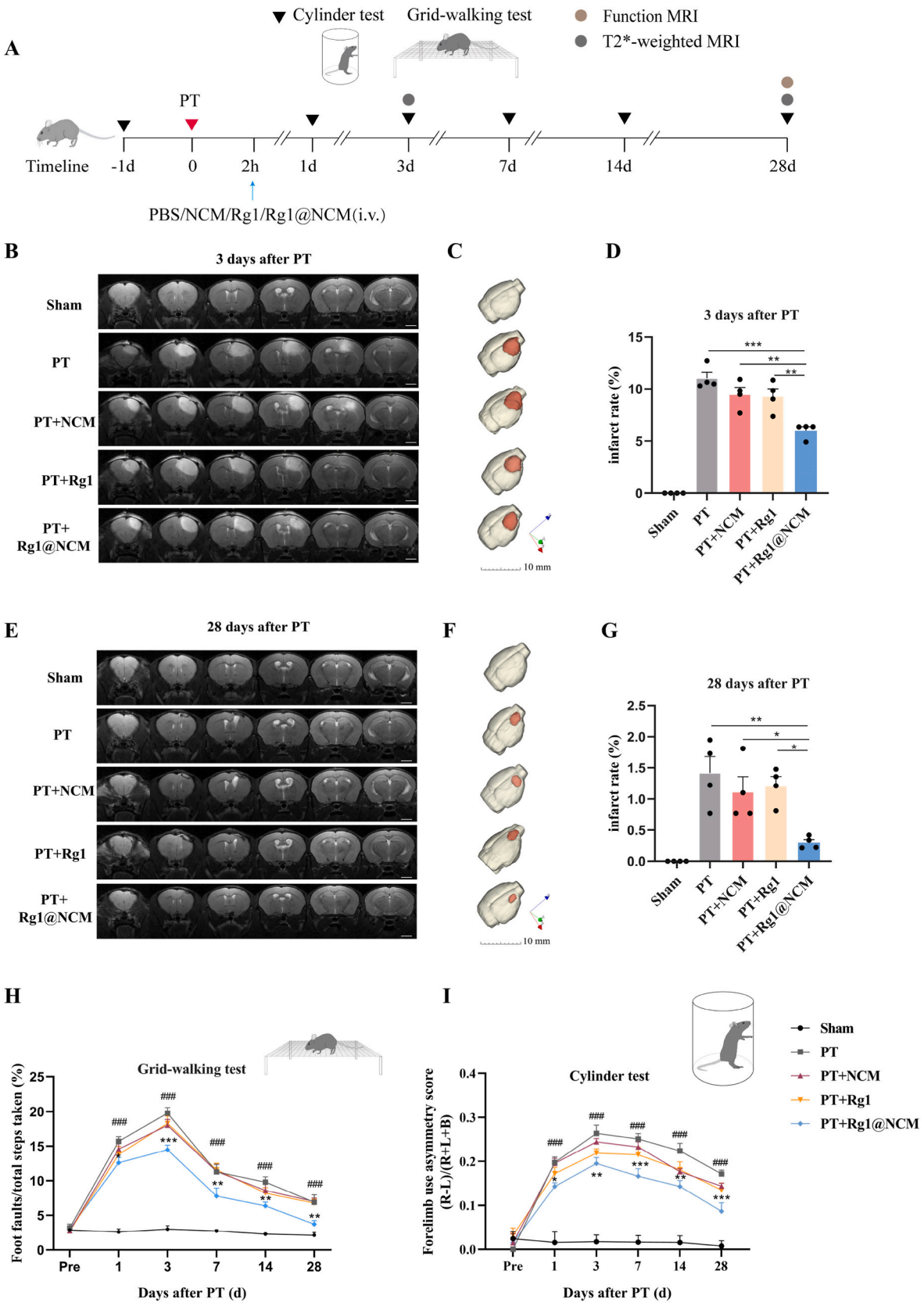

Fig. 3. Rg1@NCM alleviated the brain tissue damage and enhanced long-term functional recovery in PT mice. (A) Schematic of Rg1@NCM administration, infarction examination, and behavioral studies. Axial view of T2-weighted cerebral MR images from sham-operated and differently treated PT mice on 3 (B) or 28 (E) days after surgery. 3D reconstruction diagram of cerebral infarction volume from 3D Slicer (C, F). Infarct rate at 3 (D) or 28 (G) days after surgery (n = 4). $^{*}P < 0.05$, $^{**}P < 0.01$, $^{***}P < 0.001$. (H) The grid-walking test evaluates the motor coordination and balance functions (n = 6). (I) The cylinder test assesses their motor abilities and the use of the contralateral limb (n = 6). Scale bar = 2 mm. $^{*}P < 0.05$, $^{**}P < 0.01$, $^{***}P < 0.001$ vs. PT. $^{\#\#\#}P < 0.001$ vs. Sham.

secondary motor area (MOs), primary somatosensory area (SSp), corpus callosum (ccb), cingulum bundle (cing), and superior colliculus (SC). The Reho analysis showed that the Rg1@NCM group had higher Reho values in olfactory areas, motor cortex MO, supplemental somatosensory area (SSs), ccb, cing, cerebellum, and hippocampus compared to the NCM group (Fig. 4A). Furthermore, we selected regions of interest (ROIs) associated with stroke recovery, including the motor cortex, somatosensory cortex, and thalamus, to quantify the strength of functional connectivity between these brain regions. Enhanced functional connectivity within stroke recovery-related networks in the Rg1@NCM group was observed, as evidenced by elevated Z-scores (Fig. 4B) and visualized using BrainNet Viewer (Fig. 4C). The statistical significance of these enhancements in functional network connectivity was further confirmed by *P*-value matrices (Fig. 4D), which showed that the functional connectivity between the MOp, MOs, SSp-ul, SSp-ll, SSs, and SC was significantly stronger in the Rg1@NCM group mice compared to the NCM group (Fig. 4E). These findings suggest that the Rg1@NCM formulation was effective in promoting the functional recovery of sensorimotor and higher-order cognitive brain networks impaired by stroke. The enhanced functional connectivity in these crucial brain regions underlies the improved neurological and behavioral outcomes observed with the Rg1@NCM treatment (Fig. 3). These results highlight the potential of this nanomedicine approach to facilitate multi-faceted brain repair and functional restoration following ischemic stroke.

3.5. *Rg1@NCM promotes microglial phagocytosis of neutrophils after stroke*

To elucidate the beneficial effects of Rg1@NCM, we first investigated its impact on microglia, the primary recipient cells of the nanovesicles (Fig. 2H–I). Mice received intravenous injections of NCM or Rg1@NCM through the tail vein 2 h after PT modeling. Microglia were isolated for

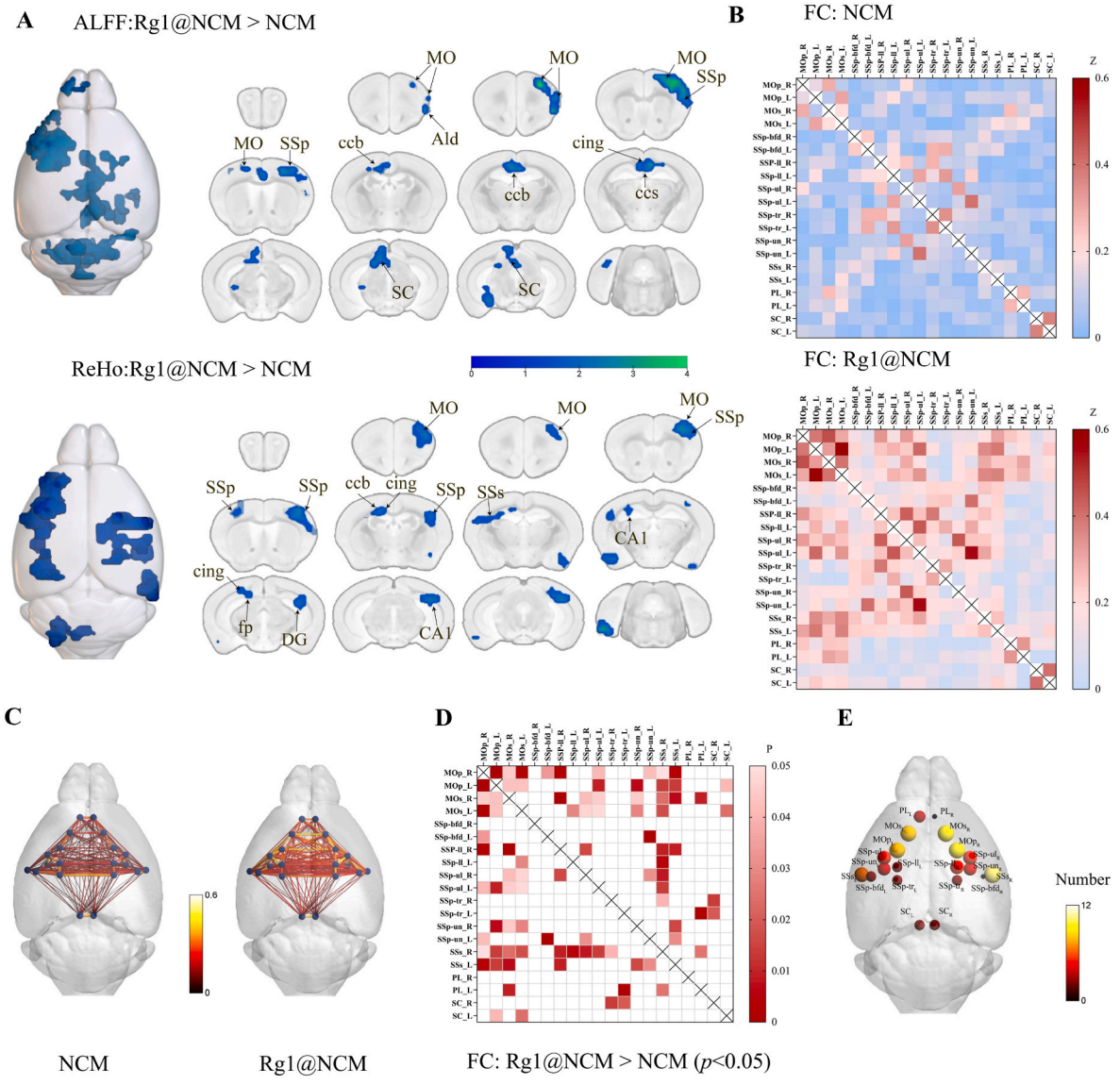

Fig. 4. Rg1@NCM improved long-term brain functional connectivity in PT mice. (A) Statistical results of ALFF and ReHo in Rg1@NCM group compared to that in NCM group. The voxel-level height threshold for ALFF was $P < 0.05$, with a cluster extent threshold of 20 voxels. The voxel-level height threshold of ReHo was $P < 0.05$ and the cluster-extent threshold was 20 voxels. Brain regions with significant differences are indicated by different colors according to T-values. (B) Heatmap of ROIs functional connectivity in mice 28 days after PT modeling (Rg1@NCM or NCM). (C) The strength of functional connectivity is represented by different sizes and colors of edges, based on the Z-values. (D) Different colors indicate ROI functional connectivity with significant enhancement according to P-values obtained from the two-sample test. (E) The size and color of the sphere represent the number of ROIs with significant differences in functionality. N = 5.

RNA-seq analysis 3 days post-injection. Compared to NCM treatment, Rg1@NCM treatment resulted in significant upregulation of 292 genes and downregulation of 155 genes (Fig. 5A). Gene ontology analysis revealed significant enrichment of biological processes (BP) associated with "cytoskeleton organization", "phagocytosis", "lysosome organization" and "ATP metabolic process" (Fig. 5B–C). To assess the morphological changes in microglia, immunofluorescence staining was performed three days post-stroke (Fig. 5D). Sholl analysis showed that PT led to a decrease in microglial branching index and maximal crossings, and there was no significant difference between the Rg1@NCM group and the PT as well as the PT + NCM groups (Fig. 5E and F), suggesting that Rg1@NCM did not further activate of microglia after PT. Nevertheless, analysis using Imaris software revealed that PT injury resulted in a decrease in microglia volume and area and an increase in spherical index. In contrast, the Rg1@NCM group showed significantly larger microglial volume and area than the PT and PT + NCM groups,

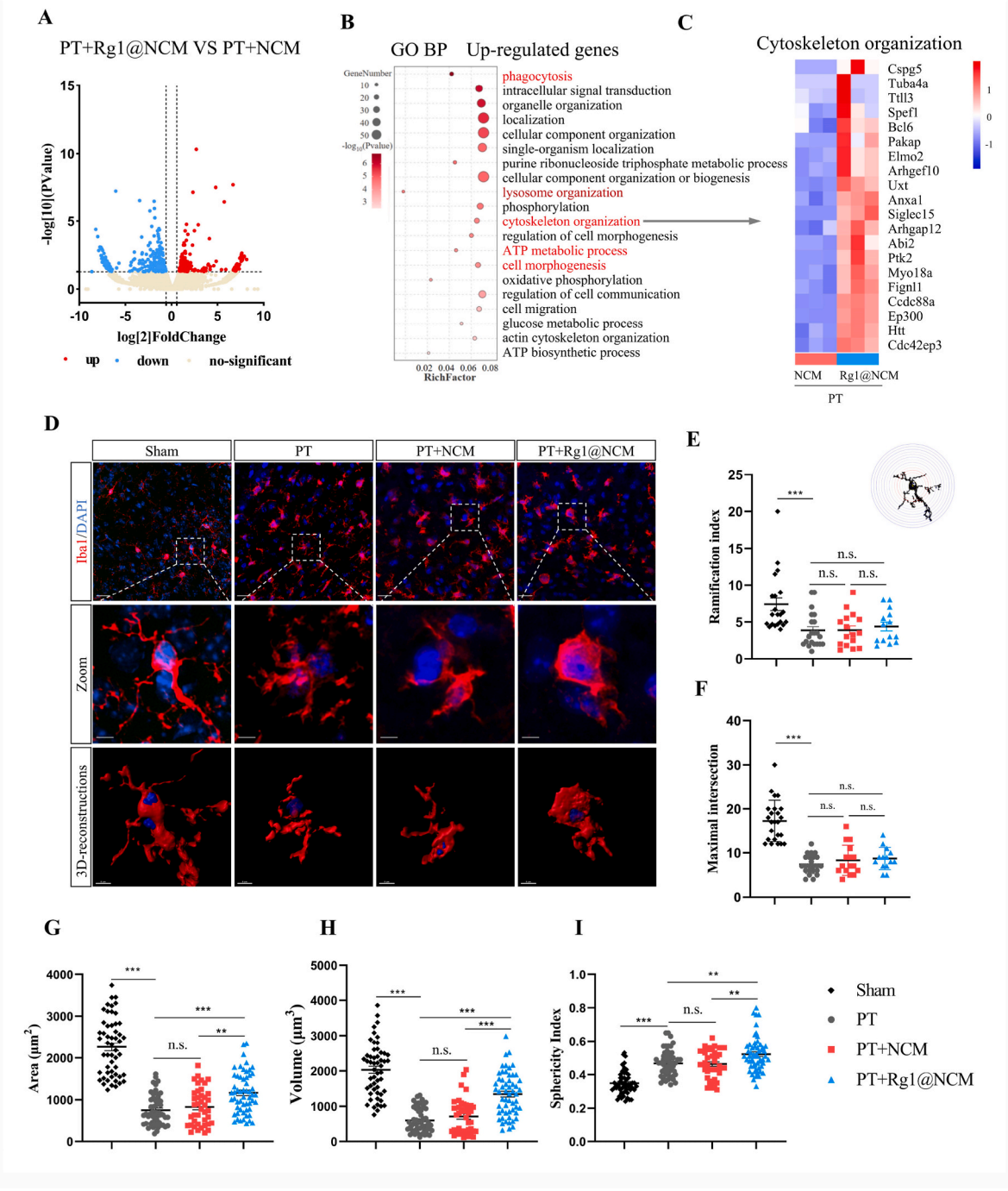

Fig. 5. Rg1@NCM altered genes and cell morphology of microglia after stroke. (A) Gene expression in freshly isolated microglia from PT model mice after injection of NCM or Rg1@NCM. Volcano plot of differentially expressed genes (DEGs) of microglia between Rg1@NCM and PBS group (n = 3). (B) Gene Ontology biological process enrichment of Up-regulated DEGs. (C) Heatmap depicting the genes profile of "Cytoskeleton organization" among the BPs. (D) Images of microglia (red) in different groups. Nuclei are stained with DAPI (blue). Confocal microscope images and 3D reconstruction (Imaris) of a representative microglial. (E, F) Sholl analysis of the above cells includes the Ramification index and Maximal intersection (n = 14–21 cells from 3 different mice). (G, H, I) Imaris analysis of the 3D reconstruction of the above cells includes the area, volume, and sphericity index (n = 41–56 cells from 3 different mice). Scale bar = 20 μm (upper), 5 μm (below). $^{*}P < 0.05$, $^{**}P < 0.01$, $^{***}P < 0.001$. n.s., no significant.

with a further increase in spherical index (Fig. 5G–I). These findings suggest that Rg1@NCM might promote the transformation of microglia to phagocytic morphology [15,34,35].

Given the observed changes in microglial morphology and gene expression, we next investigated the impact of Rg1@NCM on microglial phagocytosis of neutrophils. Microglial phagocytosis is essential for mitigating vascular and tissue damage caused by neutrophil infiltration after ischemic stroke. Our RNA-seq data revealed that Rg1@NCM treatment upregulated genes associated with "phagocytosis," "lysosome organization," and "ATP metabolic process" (Fig. 6A–C), suggesting enhanced phagocytic activity. Immunofluorescence analysis 3 days post-stroke confirmed these findings, showing a significant reduction in Ly6G$^+$ neutrophils in the brain parenchyma of Rg1@NCM-treated mice compared to both PT and NCM groups (Fig. 6D–E, H). These results confirm that Rg1@NCM effectively reduces neutrophil accumulation following ischemic stroke.

To directly assess microglial phagocytosis, we quantified the percentage of neutrophils engulfed by microglia. Consistent with previous reports demonstrating impaired microglial phagocytosis after stroke [14], only 22 % of neutrophils were phagocytosed in the PT group (Fig. 6F). Notably, Rg1@NCM treatment significantly enhanced this phagocytic rate to 64 %, whereas NCM alone had no significant effect.

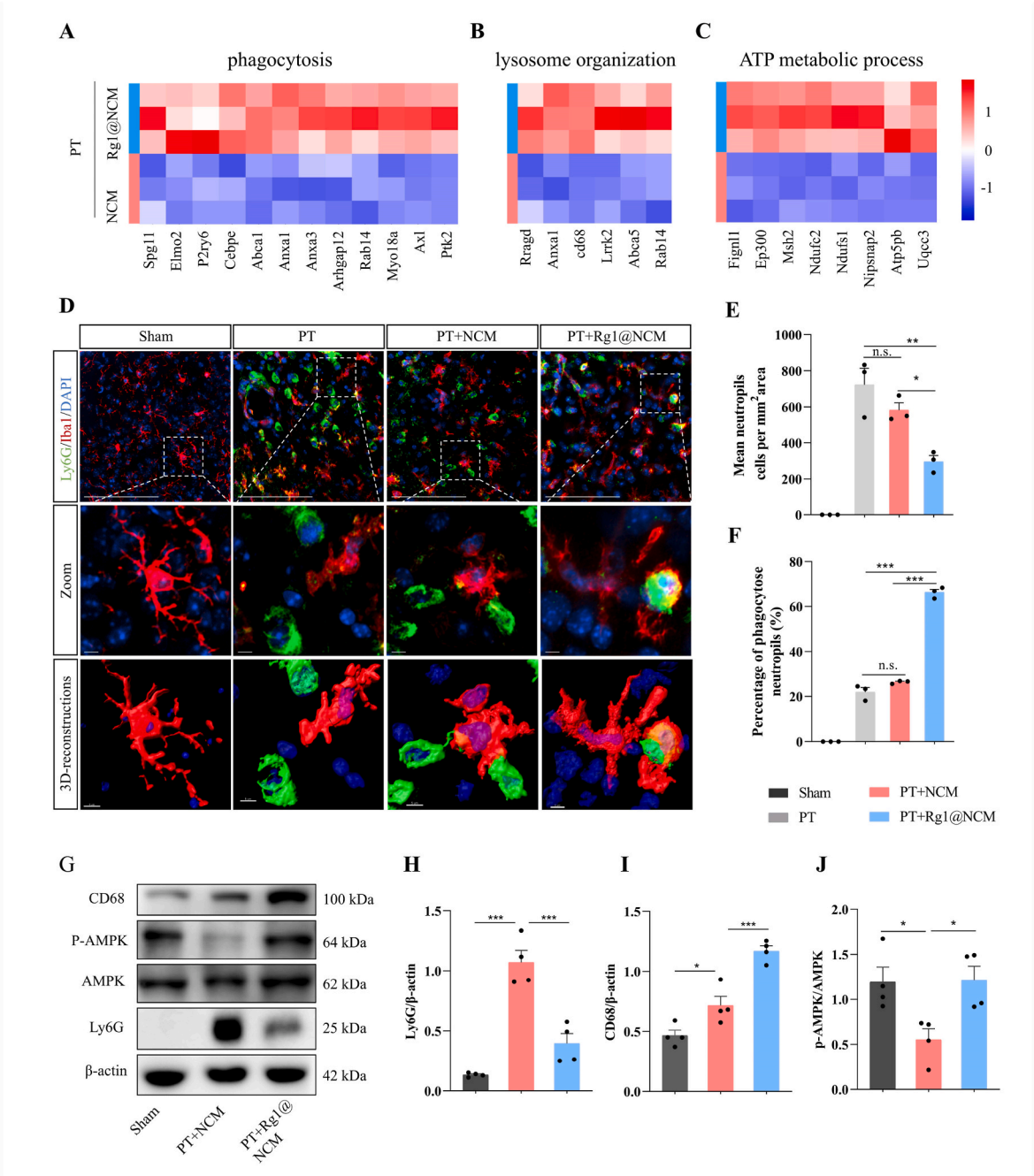

Fig. 6. Rg1@NCM promoted microglia to phagocytize neutrophils. (A) Heatmap depicting the genes profile of "phagocytosis", "lysosome organization" (B), and "ATP metabolic process" (C) among the BPs. (D) Representative images of microglia (Iba1$^+$) and neutrophils (Ly6G$^+$) of the ischemic brain on 3 days after PT. Scale bar = 200 μm. (E) The number of neutrophils (Ly6G$^+$) (n = 3). (F) The percentage of the neutrophils phagocytosed by microglia was assessed (n = 3). (G) Representative immunoblots and quantification Ly6G (H), CD68 (I), and p-AMPK/total AMPK (J), in the ischemic cortex of sham, PT + NCM and PT + Rg1@NCM groups (n = 4). Scale bar = 200 μm (upper), 5 μm (below). *$P < 0.05$, **$P < 0.01$, ***$P < 0.001$.

This enhanced phagocytic activity was further supported by increased CD68 protein levels (Fig. 6I), a marker of activated phagocytic microglia [36,37]. Given that microglial phagocytosis is an energy-intensive process requiring dynamic cytoskeletal reorganization and ATP, we investigated the involvement of AMP-activated protein kinase (AMPK), a key regulator of cellular energy homeostasis [38]. Western blot analysis revealed a significant increase in phosphorylated AMPK (p-AMPK) in the cortex of Rg1@NCM-treated mice compared to the NCM group (Fig. 6J). This finding suggests that Rg1@NCM may enhance microglial phagocytosis by upregulating AMPK signaling, thereby promoting ATP production.

3.6. Rg1@NCM enhances microglial phagocytosis of neutrophils in an AMPK-dependent manner

To further investigate the role of Rg1@NCM on microglial phagocytosis, we employed an *in vitro* co-culture system. Microglia were subjected to oxygen-glucose deprivation (OGD) to mimic ischemic and then co-cultured with neutrophils (Fig. S5). Confocal microscopy confirmed that Iba1$^+$ microglia engulfed Ly6G$^+$ neutrophils (Fig. 7A). Notably, Rg1@NCM treatment significantly enhanced the microglial phagocytic rate compared to OGD/reperfusion (OGD/R) alone (Fig. 7B). Increased protein levels of Ly6G, CD68, and p-AMPK in Rg1@NCM-treated microglia further supported this finding (Fig. 7C–F). To determine whether AMPK activation is essential for the observed effects of Rg1@NCM, we employed compound C, a specific AMPK inhibitor [39]. Seahorse analysis revealed that Rg1@NCM treatment increased basal, maximal, and ATP-linked respiration rates in microglia following OGD/R, indicating enhanced mitochondrial function (Fig. 7G–J). Compound C significantly attenuated these increases, suggesting that AMPK activity is crucial for Rg1@NCM-mediated enhancement of energy metabolism. Both imaging flow cytometry and immunofluorescence analysis demonstrated that compound C inhibited the Rg1@NCM-induced increase in microglial phagocytosis of neutrophils (Fig. 7K–M, S5B-C). Western blot analysis corroborated this inhibition, showing that compound C suppressed the Rg1@NCM-mediated upregulation of Ly6G, CD68, and p-AMPK in microglia (Figs. S5D–G). Taken together, these findings confirm that AMPK activation is necessary for Rg1@NCM to enhance energy metabolism in microglial cells and promote the phagocytosis of neutrophils.

3.7. Rg1@NCM inhibits the cGAS-STING pathway in microglia and promotes vascular remodeling after stroke

NETs released by neutrophils activate the microglial innate immune response and the release of inflammatory factors through the cGAS-STING pathway, ultimately hindering vascular remodeling and long-term functional recovery [9,12]. Given that Rg1@NCM enhances the ability of microglia to clear neutrophils, we next investigated its impact on NETs formation and the cGAS-STING pathway. RNA-seq analysis of microglia revealed downregulation of genes involved in "innate immune response" and "inflammatory response" (Fig. 8A–C). Consistent with this, Rg1@NCM treatment significantly reduced the protein levels of NETs markers (H3Cit, MPO, and NE) in the cortical tissue of mice three days post-stroke (Fig. 8D–E). Rg1@NCM treatment also suppressed the expression of key cGAS-STING pathway components, including cGAS, STING, phosphorylated TBK1 (p-TBK1), and phosphorylated IRF3 (p-IRF3) (Fig. 8F and G). Consequently, Rg1@NCM also inhibited the downstream production of pro-inflammatory cytokines IL-6 (Fig. 8F and G) and IFN-β (Fig. 8H). Preserving BBB integrity is crucial for post-stroke recovery, and BBB disruption is often associated with cGAS-STING activation [40]. Notably, Rg1@NCM treatment increased the expression of tight junction proteins ZO-1 and Occludin, essential for BBB integrity, in the injured brain (Fig. 8I–J). Endogenous vascular regeneration typically occurs within 4–7 days after ischemic stroke, and vascular maturation usually occurs after 14 days [4]. Therefore, to assess the long-term impact of Rg1@NCM on vascular remodeling, we examined cerebral microvasculature 14 days post-stroke. Rg1@NCM treatment significantly increased vessel density, perfused microvascular (diameter <6 μm) length, contact area, volume, and volume/total perfused volume ratio in the peri-infarct cortex, while no significant differences were observed between the stroke and NCM groups (Fig. 8K–P). These findings demonstrate that Rg1@NCM effectively inhibits the cGAS-STING pathway in microglia, likely due to its ability to enhance neutrophil clearance and reduce NETs formation. This, in turn, contributes to a more favorable microenvironment for vascular remodeling and tissue repair, highlighting the therapeutic potential of Rg1@NCM for promoting post-stroke recovery (see Fig. 9).

4. Discussion

Overcoming the BBB remains a significant challenge in developing effective therapeutics for ischemic stroke. While Rg1 shows promise in preclinical models, its therapeutic translation is hindered by low bioavailability and poor BBB penetration [18,41]. To address this, we exploited the inherent inflammatory targeting of neutrophils by developing Rg1-loaded neutrophil cell membrane vesicles (NCM) for targeted delivery to the ischemic brain.

Rg1-loaded NCM exhibited an average size of ~140 nm, facilitating BBB penetration [42,43]. Importantly, NCM retained key adhesion molecules, including PSGL-1 and integrin β2, essential for neutrophil adhesion to inflamed endothelium [28,44,45], enabling targeted delivery to the ischemic brain. Indeed, *in vivo* multiphoton microscopy revealed NCM accumulation within the infarct region, specifically around blood vessels and in association with microglia. Increased DiD and Rg1 accumulation in the ischemic hemisphere further confirmed this targeting. More than 80 % of NCM are taken up by microglia after injection 3 h. It is worth noting that NCM release less Rg1 in serum within the first 3 h, mainly releasing it between 3 and 24 h (Fig. S1), which may indicate a relatively stable state of the vesicles before reaching the site of injury, and then a substantial release of Rg1 upon arrival at the site of injury and taken up by microglial cells. These results suggest Rg1@NCM could be targeted delivery and potential taken up by microglia within the ischemic region.

Consistent with its enhanced delivery, Rg1@NCM significantly reduced infarct volume and improved neurological function up to 28 days post-stroke, surpassing the efficacy of free Rg1 or empty NCM (Fig.3). These findings highlight the importance of targeted delivery, as 10 mg/kg free Rg1, a dose comparable to previous studies [17,21,46,47], showed limited efficacy. fMRI revealed that Rg1@NCM enhanced brain activity (ALFF, ReHo) and functional connectivity within motor and sensorimotor regions, corroborating the observed behavioral improvements (Fig. 3H and I). Enhanced functional connectivity within the motor cortex network (MOp-MOs, SSp-ul, SSp-ll, SSs, SC) further supports the beneficial effects of Rg1@NCM on long-term functional recovery.

Given the detrimental role of NETs and microglial cGAS-STING activation in stroke recovery [9,10], we investigated the impact of Rg1@NCM on these processes. Our findings demonstrate that Rg1@NCM promotes microglial phagocytosis of neutrophils, reducing NETs accumulation and downstream cGAS-STING activation, and improves post-stroke vascular remodeling. Mechanistically, Rg1@NCM enhanced AMPK phosphorylation in microglia, leading to increased cellular respiration and ATP production, ultimately promoting phagocytosis. Notably, the AMPK inhibitor compound C attenuated these effects, highlighting the crucial role of AMPK in Rg1@NCM-mediated neuroprotection.

To address potential concerns about excessive microglial phagocytosis and neuronal engulfment, we also examined neuronal changes in the context of enhanced microglial phagocytosis. Neurons (NeuN, red), unhealthy cells (TUNEL, green), and microglia (Iba1, cyan) were visualized (Fig. S6A). In the sham group, microglia exhibited a surveillance

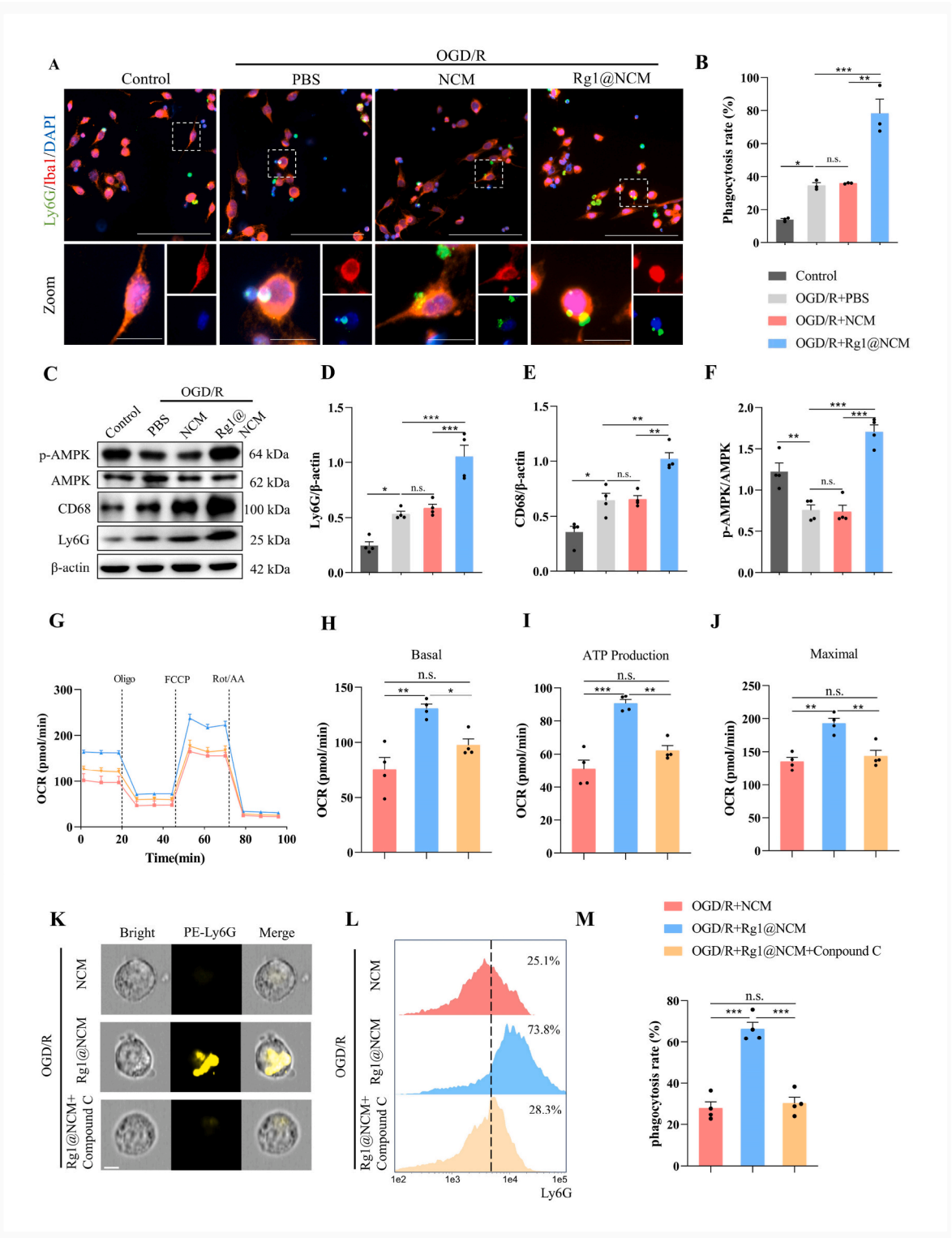

Fig. 7. Rg1@NCM activated AMPK to promote the phagocytosis of neutrophils by microglial cells after OGD/R. (A) Representative images of BV2 microglia (Iba1^{+}) and primary neutrophils (Ly6G^{+}) of different groups (control, OGD/R, OGD/R + NCM, OGD/R + Rg1@NCM). Scale bar = 100 μm (upper), 20 μm (below). (B) The percentage of microglial phagocytic neutrophils (n = 3). (C) Representative immunoblots and quantification Ly6G (D), CD68 (E), and p-AMPK/total AMPK (F) in the microglial cells after co-incubation in the different groups (n = 4). (G) After OGD/R, BV2 microglia were incubated with Rg1@NCM and compound C (or NCM). BV2 was assayed for baseline (H), ATP-production (I), and maximal (J) respiration using a Seahorse analyzer (n = 4). (K) Representative immunofluorescence images of Ly6G-positive cells revealed by imaging flow cytometry. (L, M) The phagocytosis ratio of neutrophils by microglia was detected by IDEAS analysis (n = 4). Scale bar = 10 μm *$P < 0.05$, **$P < 0.01$, ***$P < 0.001$.

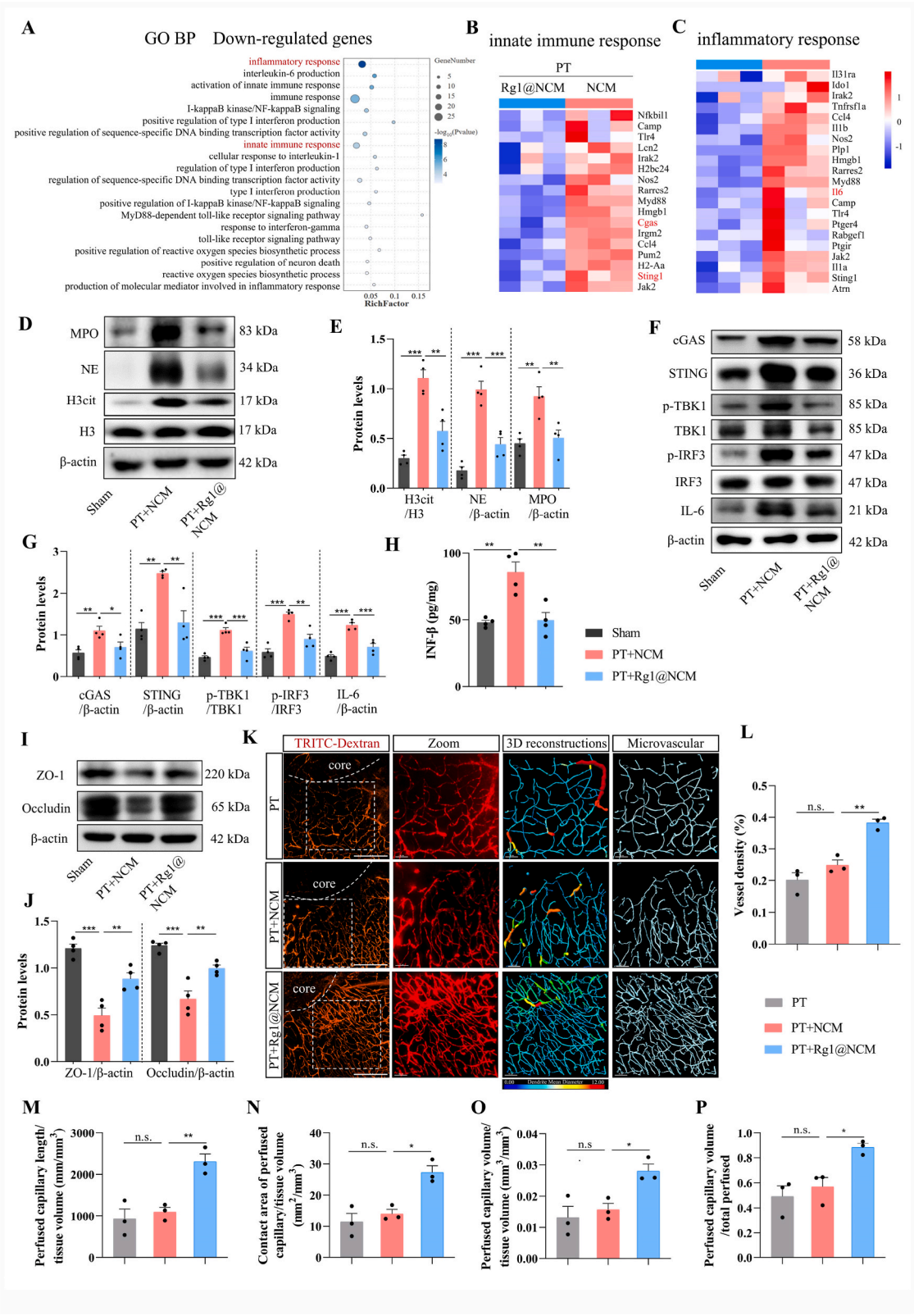

Fig. 8. Rg1@NCM inhibited the cGAS-STING pathway of microglia and promoted vascular remodeling after stroke. (A) Gene Ontology biological process enrichment of down-regulated DEGs. (B, C) Heatmap depicting gene profile of "innate immune response" and "inflammatory response" among the BPs. (D, E) Representative immunoblots and quantification for H3Cit, NE, and MPO expression in the ischemic cortex of sham and PT + NCM and PT + Rg1@NCM (n = 4). (F, G) Representative immunoblots and quantification for cGAS, STING, pTBK1, total TBK1, pIRF3, total IRF3, and IL-6 expression in the ischemic cortex. (H) Elisa assay to determine the content of IFN-β in damaged brain tissue (n = 4). (I, J) ZO-1 and Occludin expression in the ischemic cortex (n = 4). (K–P) Representative images with TRITC-Dextran 155 kDa showing blood vessels in the peri-infarct cortex at day 14 after PT in mice, followed by the analysis of vascular density, perfused capillary length (Diameter less than 6 μm), contact area of perfused capillary, perfused capillary volume/total volume, and perfused capillary volume/total perfused (n = 3). All data represent as Mean ± SEM. $^{*}P < 0.05$, $^{**}P < 0.01$, $^{***}P < 0.001$. Scale bar = 200 μm (left), 50 μm (right).

phenotype, closely associated with neuronal cell bodies. Post-PT, microglia displayed morphological changes consistent with activation, but remained associated with healthy neurons ($NeuN^+/TUNEL^-$) in all treatment groups. No evidence of aberrant phagocytosis of healthy neurons was observed following Rg1@NCM treatment. We examined neuronal density at the infarct periphery 28 days post-stroke. As shown in Fig. S7, no significant difference was observed between the Rg1@NCM and PT control groups, suggesting that Rg1@NCM treatment does not exacerbate neuronal loss. Besides, at 3 days post-PT, the proportion of microglia phagocytosing apoptotic neurons ($NeuN^+/TUNEL^+$) was consistently lower than the proportion phagocytosing neutrophils across all groups. While Rg1@NCM treatment showed a trend towards increased phagocytosis of apoptotic neurons, this difference was not statistically significant compared to the PT group. However, Rg1@NCM did significantly enhanced microglial phagocytosis of neutrophils (Fig. S6B). This suggests that Rg1@NCM may selectively enhance microglial phagocytosis of neutrophils, but not neurons, after PT. The mechanism behind this selective effect is unclear, but it may involve early uptake of neutrophil vesicles activating recognition pathways, with Rg1 providing the energy needed for subsequent neutrophils phagocytosis by microglia.

We validated NCM's safety profile in both *in vitro* and *in vivo* studies. NCM showed no significant cytotoxicity against BV2 cells at concentrations up to 250 μg/mL (Fig. S8A). Following injection, NCM was primarily distributed to the liver, spleen, and kidneys (Fig. S2). No pathological damage was observed in these organs after 3 days of NCM treatment, as assessed by H&E staining (Fig. S8B). Additionally, HE staining of brain slices 28 days after PT surgery showed similar conditions in the cortical cells of the NCM group compared to the PT and free Rg1 groups, indicating no further neurotoxicity due to NCM (Fig. S7). These results demonstrate the excellent biocompatibility of NCM.

5. Conclusion

This study presents a novel drug delivery system utilizing neutrophil cell membrane vesicles for targeted Rg1 delivery to the ischemic brain. Our findings demonstrate that Rg1@NCM effectively enhances Rg1 delivery across the BBB, leading to increased Rg1 accumulation within the ischemic hemisphere. This targeted approach significantly reduced infarct volume and improved long-term functional recovery in a photothrombotic stroke model, outperforming free Rg1 at a same dose, highlighting the critical role of targeted delivery in maximizing therapeutic efficacy. Mechanistically, Rg1@NCM leverages the inflammatory targeting of neutrophils and their subsequent phagocytosis by microglia within the ischemic brain. This facilitates Rg1 delivery, promoting microglial phagocytosis of neutrophils and mitigating the detrimental effects of NETs formation. Consequently, Rg1@NCM suppresses the cGAS-STING pathway, reduces neuroinflammation, promotes BBB integrity, and enhances vascular remodeling (Fig. 9). This study highlights the therapeutic potential of reprogramming microglia to enhance their endogenous repair capabilities, offering a promising therapeutic avenue for ischemic stroke management. By selectively augmenting beneficial microglial functions, this approach may effectively mitigate neurological dysfunction damage and promote functional recovery after stroke.

CRediT authorship contribution statement

Kaichao Hu: Writing – original draft, Visualization, Methodology, Formal analysis, Data curation, Conceptualization. **Junrui Ye:** Methodology, Data curation. **Pinglong Fan:** Visualization, Data curation. **Ruifang Zheng:** Methodology, Data curation. **Shasha Wang:** Methodology, Data curation. **Ye Peng:** Methodology, Data curation. **Yuan**

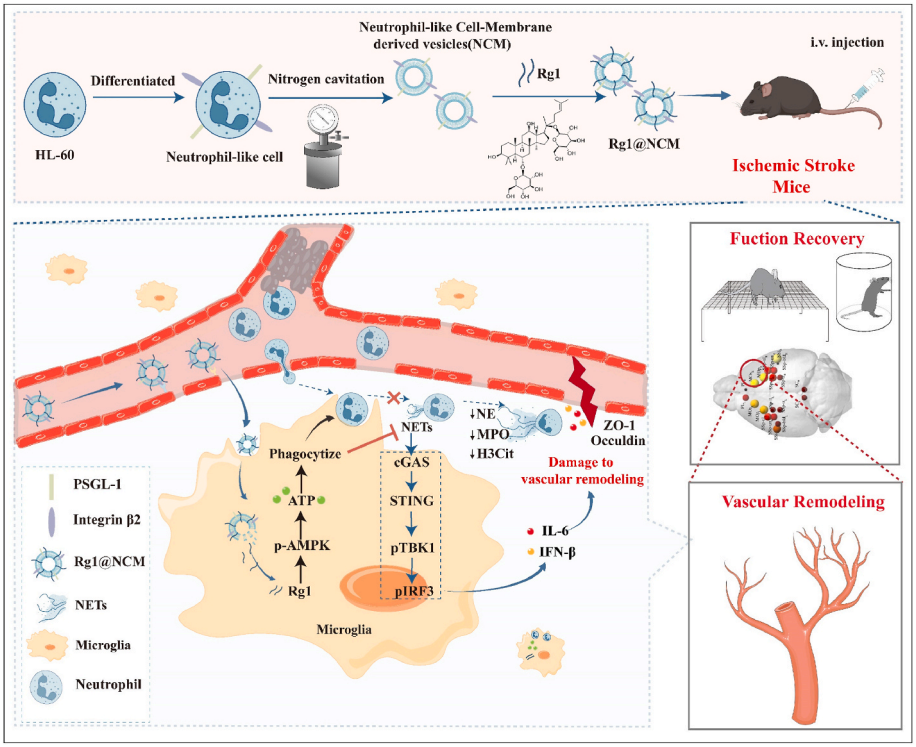

Fig. 9. Illustration of neutrophil-like cell membrane-derived vesicles carrying ginsenoside Rg1 offer a promising therapeutic strategy for targeted ischemic stroke therapy. Rg1@NCM targets the infarct border zone, interacting with the inflamed endothelium and crossing the blood-brain barrier. Uptake of Rg1@NCM by microglia activates AMPK signaling, which enhances microglial phagocytosis of neutrophils, attenuates NETs formation, and downregulates the cGAS-STING pathway, thereby reducing IL-6 and IFN-β production. Furthermore, Rg1@NCM upregulates tight junction proteins (ZO-1 and occludin), promoting vascular repair. Collectively, these actions contribute to functional recovery after ischemic stroke, highlighting the potential of Rg1@NCM as a therapeutic strategy for targeted reprogramming microglia toward a neuroprotective phenotype and promoting endogenous brain repair.

Ruan: Visualization, Data curation. **Xu Yan:** Project administration, Data curation. **Zhao Zhang:** Writing – review & editing, Writing – original draft, Project administration, Methodology, Data curation, Conceptualization. **Shifeng Chu:** Writing – review & editing, Conceptualization. **Naihong Chen:** Writing – review & editing, Resources, Project administration, Funding acquisition, Conceptualization.

Ethics approval and consent to participate

SPF-grade male C57BL/6J mice (9 weeks old, weight = 23 ± 2 g) were purchased from Beijing SPF Biotechnology Co., Ltd. The mice were housed in a 12-h light/dark cycle and had ad libitum access to water and standard laboratory chow. All animal protocols were approved by the Ethics Committee of the Animal Center of the Chinese Academy of Medical Sciences. All animal care and experimental procedures complied with the principles outlined in the NIH Guide for the Care and Use of Laboratory Animals and were approved by the Institutional Animal Care and Use Committee of the Peking Union Medical College and Chinese Academy of Medical Sciences (Ethics number: 00007889).

Declaration of competing interest

The authors affirm that they have no known financial or interpersonal conflicts that could have appeared to have an impact on the research presented in this study.

Acknowledgments

This study was supported by the National Natural Science Foundation of China (U2202214, 82074044, 82374060, U21A20410), the National Key R&D Program of China (2022YFC3500300), the CAMS Innovation Fund for Medical Sciences (CIFMS) (2021-I2M-1–020).

Appendix A. Supplementary data

Supplementary data to this article can be found online at https://doi.org/10.1016/j.bioactmat.2025.01.017.

References

[1] Global, regional, and national burden of stroke and its risk factors, 1990-2019: a systematic analysis for the Global Burden of Disease Study 2019, Lancet Neurol. 20 (10) (2021) 795–820.
[2] W. Hacke, M. Kaste, E. Bluhmki, et al., Thrombolysis with alteplase 3 to 4.5 hours after acute ischemic stroke, N. Engl. J. Med. 359 (13) (2008) 1317–1329.
[3] P. Khandelwal, D.R. Yavagal, R.L. Sacco, Acute ischemic stroke intervention, J. Am. Coll. Cardiol. 67 (22) (2016) 2631–2644.
[4] B. Li, W. Xi, Y. Bai, et al., FTO-dependent m(6)A modification of Plpp3 in circSCMH1-regulated vascular repair and functional recovery following stroke, Nat. Commun. 14 (1) (2023) 489.
[5] J. Krupinski, J. Kaluza, P. Kumar, S. Kumar, J.M. Wang, Role of angiogenesis in patients with cerebral ischemic stroke, Stroke 25 (9) (1994) 1794–1798.
[6] J. Fang, Z. Wang, C.Y. Miao, Angiogenesis after ischemic stroke, Acta Pharmacol. Sin. 44 (7) (2023) 1305–1321.
[7] P. Sun, K. Zhang, S.H. Hassan, et al., Endothelium-targeted deletion of microRNA-15a/16-1 promotes poststroke angiogenesis and improves long-term neurological recovery, Circ. Res. 126 (8) (2020) 1040–1057.
[8] R. Rust, Insights into the dual role of angiogenesis following stroke, J. Cerebr. Blood Flow Metabol. 40 (6) (2020) 1167–1171.
[9] L. Kang, H. Yu, X. Yang, et al., Neutrophil extracellular traps released by neutrophils impair revascularization and vascular remodeling after stroke, Nat. Commun. 11 (1) (2020) 2488.
[10] R. Wang, Y. Zhu, Z. Liu, et al., Neutrophil extracellular traps promote tPA-induced brain hemorrhage via cGAS in mice with stroke, Blood 138 (1) (2021) 91–103.
[11] F. Denorme, I. Portier, J.L. Rustad, et al., Neutrophil extracellular traps regulate ischemic stroke brain injury, J. Clin. Invest. 132 (10) (2022) e154225.
[12] Z. Zhao, Z. Pan, S. Zhang, et al., Neutrophil extracellular traps: a novel target for the treatment of stroke, Pharmacol. Ther. 241 (2023) 108328.
[13] J. Neumann, S. Henneberg, S. von Kenne, et al., Beware the intruder: Real time observation of infiltrated neutrophils and neutrophil-Microglia interaction during stroke in vivo, PLoS One 13 (3) (2018) e0193970.
[14] L. Li, S.Q. Cheng, Y.Q. Sun, et al., Resolvin D1 reprograms energy metabolism to promote microglia to phagocytize neutrophils after ischemic stroke, Cell Rep. 42 (6) (2023) 112617.
[15] A. Otxoa-de-Amezaga, F. Miró-Mur, J. Pedragosa, et al., Microglial cell loss after ischemic stroke favors brain neutrophil accumulation, Acta Neuropathol. 137 (2) (2019) 321–341.
[16] W.Y. Ma, Q.L. Wu, S.S. Wang, et al., A breakdown of metabolic reprogramming in microglia induced by CKLF1 exacerbates immune tolerance in ischemic stroke, J. Neuroinflammation 20 (1) (2023) 97.
[17] M. Lin, W. Sun, W. Gong, Y. Ding, Y. Zhuang, Q. Hou, Ginsenoside Rg1 protects against transient focal cerebral ischemic injury and suppresses its systemic metabolic changes in cerabral injury rats, Acta Pharm. Sin. B 5 (3) (2015) 277–284.
[18] W. Xie, P. Zhou, Y. Sun, et al., Protective effects and target network analysis of ginsenoside Rg1 in cerebral ischemia and reperfusion injury: a comprehensive overview of experimental studies, Cells 7 (12) (2018).
[19] J. Chen, X. Zhang, X. Liu, et al., Ginsenoside Rg1 promotes cerebral angiogenesis via the PI3K/Akt/mTOR signaling pathway in ischemic mice, Eur. J. Pharmacol. 856 (2019) 172418.
[20] Z.C. Xi, H.G. Ren, L. Ai, et al., Ginsenoside Rg1 mitigates cerebral ischaemia/reperfusion injury in mice by inhibiting autophagy through activation of mTOR signalling, Acta Pharmacol. Sin. (2024).
[21] L. Feng, L. Wang, C. Hu, X. Jiang, Pharmacokinetics, tissue distribution, metabolism, and excretion of ginsenoside Rg1 in rats, Arch Pharm. Res. (Seoul) 33 (12) (2010) 1975–1984.
[22] Y. Gu, K. Ren, L. Wang, C. Jiang, Q. Yao, Rg1 in combination with mannitol protects neurons against glutamate-induced ER stress via the PERK-eIF2 α-ATF4 signaling pathway, Life Sci. 263 (2020) 118559.
[23] J. Shen, Z. Zhao, W. Shang, et al., Ginsenoside Rg1 nanoparticle penetrating the blood-brain barrier to improve the cerebral function of diabetic rats complicated with cerebral infarction, Int. J. Nanomed. 12 (2017) 6477–6486.
[24] W. Shang, X. Zhao, F. Yang, et al., Ginsenoside Rg1 nanoparticles induce demethylation of H3K27me3 in VEGF-A and jagged 1 promoter regions to activate angiogenesis after ischemic stroke, Int. J. Nanomed. 17 (2022) 5447–5468.
[25] L. Garcia-Bonilla, Z. Shahanoor, R. Sciortino, et al., Analysis of brain and blood single-cell transcriptomics in acute and subacute phases after experimental stroke, Nat. Immunol. 25 (2) (2024) 357–370.
[26] J. Neumann, M. Riek-Burchardt, J. Herz, et al., Very-late-antigen-4 (VLA-4)-mediated brain invasion by neutrophils leads to interactions with microglia, increased ischemic injury and impaired behavior in experimental stroke, Acta Neuropathol. 129 (2) (2015) 259–277.
[27] L. Kang, H. Yu, X. Yang, et al., Neutrophil extracellular traps released by neutrophils impair revascularization and vascular remodeling after stroke, Nat. Commun. 11 (1) (2020) 2488.
[28] D. Chu, X. Dong, X. Shi, C. Zhang, Z. Wang, Neutrophil-based drug delivery systems, Adv. Mater. 30 (22) (2018) e1706245.
[29] A. Zarbock, K. Ley, R.P. McEver, A. Hidalgo, Leukocyte ligands for endothelial selectins: specialized glycoconjugates that mediate rolling and signaling under flow, Blood 118 (26) (2011) 6743–6751.
[30] Y. Zhao, Q. Li, J. Niu, et al., Neutrophil membrane-camouflaged polyprodrug nanomedicine for inflammation suppression in ischemic stroke therapy, Adv. Mater. 36 (21) (2024) e2311803.
[31] R. Sun, M. Wang, T. Zeng, et al., Scaffolds functionalized with matrix metalloproteinase-responsive release of miRNA for synergistic magnetic hyperthermia and sensitizing chemotherapy of drug-tolerant breast cancer, Bioact. Mater. 44 (2025) 205–219.
[32] M. Dahiya, R. Awasthi, G. Gupta, et al., Optimization studies on imatinib mesylate loaded nanoliposomes using box-behnken design, Nano Biomedicine and Engineering 14 (1) (2022) 23–37.
[33] Q. Chen, J. Zhou, H. Zhang, et al., One-step analysis of brain perfusion and function for acute stroke patients after reperfusion: a resting-state fMRI study, J. Magn. Reson. Imag. 50 (1) (2019) 221–229.
[34] N. Stence, M. Waite, M.E. Dailey, Dynamics of microglial activation: a confocal time-lapse analysis in hippocampal slices, Glia 33 (3) (2001) 256–266.
[35] F.R. Walker, S.B. Beynon, K.A. Jones, et al., Dynamic structural remodelling of microglia in health and disease: a review of the models, the signals and the mechanisms, Brain Behav. Immun. 37 (2014) 1–14.
[36] J. Cheng, R. Zhang, Z. Xu, et al., Early glycolytic reprogramming controls microglial inflammatory activation, J. Neuroinflammation 18 (1) (2021) 129.
[37] B.V. Lananna, C.A. McKee, M.W. King, et al., Chi3l1/YKL-40 is controlled by the astrocyte circadian clock and regulates neuroinflammation and Alzheimer's disease pathogenesis, Sci. Transl. Med. 12 (574) (2020).
[38] D.G. Hardie, B.E. Schaffer, A. Brunet, AMPK: an energy-sensing pathway with multiple inputs and outputs, Trends Cell Biol. 26 (3) (2016) 190–201.
[39] S. Saito, A. Furuno, J. Sakurai, H.R. Park, K. Shin-ya, A. Tomida, Compound C prevents the unfolded protein response during glucose deprivation through a mechanism independent of AMPK and BMP signaling, PLoS One 7 (9) (2012) e45845.
[40] X. Zong, Y. Li, C. Liu, et al., Theta-burst transcranial magnetic stimulation promotes stroke recovery by vascular protection and neovascularization, Theranostics 10 (26) (2020) 12090–12110.
[41] S.J. Yang, J.J. Wang, P. Cheng, L.X. Chen, J.M. Hu, G.Q. Zhu, Ginsenoside Rg1 in neurological diseases: from bench to bedside, Acta Pharmacol. Sin. 44 (5) (2023) 913–930.
[42] G.C. Terstappen, A.H. Meyer, R.D. Bell, W. Zhang, Strategies for delivering therapeutics across the blood-brain barrier, Nat. Rev. Drug Discov. 20 (5) (2021) 362–383.
[43] J.V. Georgieva, D. Hoekstra, I.S. Zuhorn, Smuggling drugs into the brain: an overview of ligands targeting transcytosis for drug delivery across the blood-brain barrier, Pharmaceutics 6 (4) (2014) 557–583.

[44] M. Phillipson, P. Kubes, The neutrophil in vascular inflammation, Nat. Med. 17 (11) (2011) 1381–1390.
[45] X. Dong, J. Gao, C.Y. Zhang, C. Hayworth, M. Frank, Z. Wang, Neutrophil membrane-derived nanovesicles alleviate inflammation to protect mouse brain injury from ischemic stroke, ACS Nano 13 (2) (2019) 1272–1283.
[46] L. Wang, H. Zhao, Z.Z. Zhai, L.X. Qu, Protective effect and mechanism of ginsenoside Rg1 in cerebral ischaemia-reperfusion injury in mice, Biomed. Pharmacother. 99 (2018) 876–882.
[47] S.F. Chu, Z. Zhang, X. Zhou, et al., Ginsenoside Rg1 protects against ischemic/reperfusion-induced neuronal injury through miR-144/Nrf2/ARE pathway, Acta Pharmacol. Sin. 40 (1) (2019) 13–25.

Abbreviations

STING: Stimulator of interferon genes
cGAS: Cyclic GMP–AMP synthase
TBK1: TANK-binding kinase 1
IRF3: Interferon regulatory factor 3
IFN-β: Interferon β
Iba1: Ionized calcium-binding adapter molecule1
NCM: neutrophil-like cell membrane-derived vesicles
PT: photothrombotic
NETs: neutrophil extracellular traps
BBB: blood-brain barrier
PSGL-1: P-selectin glycoprotein ligand-1
AMPK: Adenosine 5'-monophosphate (AMP)-activated protein kinase